

The dramatic transition of the extreme Red Supergiant WOH G64 to a Yellow Hypergiant

G. Muñoz-Sanchez^{1,2}, M. Kalitsounaki^{1,2}, S. de Wit^{1,2}, K. Antoniadis^{1,2}, A.Z. Bonanos¹, E. Zapartas³,
K. Boutsia^{4,5}, E. Christodoulou^{1,2}, G. Maravelias^{1,3}, I. Soszyński⁶, and A. Udalski⁶

¹ IAASARS, National Observatory of Athens, I. Metaxa & Vas. Pavlou St., 15236, Penteli, Athens, Greece

² Department of Physics, National and Kapodistrian University of Athens, Panepistimiopolis, Zografos, 15784, Greece

³ Institute of Astrophysics, FORTH, GR-71110, Heraklion, Greece

⁴ Cerro Tololo Inter-American Observatory/NSF NOIRLab, Casilla 603, La Serena, Chile

⁵ Las Campanas Observatory, Carnegie Observatories, Colina El Pino, Casilla 601, La Serena, Chile

⁶ Astronomical Observatory, University of Warsaw, Al. Ujazdowskie 4, 00-478 Warszawa, Poland

ABSTRACT

Red Supergiants (RSGs) are cool, evolved massive stars in the last evolutionary stage before exploding as a supernova. However, the most luminous RSGs may evolve blueward before exploding, given the observational evidence for luminous, warm, post-RSG objects and the lack of supernova progenitors originating from luminous RSGs. In this work, we analyze WOH G64, considered since the 1980s as the most extreme RSG in the Large Magellanic Cloud in terms of its size, luminosity, and mass-loss rate. Time-series photometry over the last 30 years reveals a sudden, yet smooth change from semi-regular to irregular variability in 2014. Multi-epoch optical spectroscopy confirms the transition, as WOH G64 now exhibits properties of a B[e] star in the optical, and warm-star features in the near-infrared. We report that WOH G64 has transitioned from a RSG to a Yellow Hypergiant and, moreover, has a B-star companion. The dramatic transition can be explained by: a) binary interactions partially stripping the envelope, b) the return of WOH G64 to a quiescent state after an outstanding eruption exceeding 30 years, and c) the expulsion of its outer layers due to a pre-SN superwind phase, indicating its imminent explosion. WOH G64 offers a unique opportunity to witness stellar evolution in real time, providing crucial clues for the late phases of massive stars and their resulting supernovae.

Key words. Stars: individual: WOH G64 - stars: massive - stars: supergiants - stars: atmospheres - stars: late-type - stars: mass-loss

1. Introduction

Red supergiants (RSGs) are cool, evolved massive stars with initial masses (M_{ini}) between 8 – 25 M_{\odot} (Meynet & Maeder 2003; Ekström et al. 2012; Levesque 2017). The RSG phase is considered the latest evolutionary stage before either exploding as a Type-II Supernova (SN) or collapsing into a black hole (Smartt 2009; Sukhbold et al. 2016; O’Connor & Ott 2011; Adams et al. 2017). Nevertheless, several studies have suggested the existence of post-RSG objects (e.g., see review by Gordon & Humphreys 2019, and references therein), based on the large quantities of dust observed surrounding some Blue and Yellow Supergiants (BSGs and YSGs). Their dust is thought to result from enhanced periods of mass loss during the previous RSG phase. Specifically, Yellow Hypergiants (YHG, de Jager 1998) are very luminous YSGs exhibiting significant infrared (IR) excess. They are considered strong candidates for post-RSG objects due to their complex circumstellar environments, high mass-loss rates, and episodic ejections, such as IRC +10420 (Oudmaijer et al. 1996), IRAS 17163-3907 or ‘Fried Egg Nebula’ (Koumpia et al. 2020), and Var A in M33 (Humphreys et al. 2006).

The physical mechanism and the conditions under which a star evolves into a post-RSG phase, however, remain uncertain. Stellar evolution models reveal that strong stationary winds could strip the envelope of the RSGs to drive their evolution to a warmer phase (e.g., Meynet et al. 2015; Zapartas et al. 2024). Nevertheless, most empirical relations (e.g., de Jager et al. 1988; Beasor et al. 2020; Antoniadis et al. 2024; Decin et al. 2024)

find weaker stationary winds, preventing the formation of post-RSG objects. Detections of clumpy and asymmetric material in the circumstellar medium (CSM) of luminous RSGs indicate that episodic mass ejections might play a significant role (e.g. NML Cyg, VY CMa, Betelgeuse; Richards et al. 1996; Decin et al. 2006; Humphreys et al. 2007; Dupree et al. 2022). These ejections are associated with asymmetric gaseous outflows related to surface activity (Humphreys & Jones 2022), which can be detected as dimming events if the ejection occurs in the line-of-sight (e.g., Betelgeuse, RW Cep, and [W60] B90; Guinan et al. 2019; Montargès et al. 2021; Anugu et al. 2023; Muñoz-Sanchez et al. 2024). Unfortunately, the impact of episodic mass loss on RSG evolution remains uncertain because its significance varies among RSGs (Humphreys & Jones 2022) and is not included in mass-loss prescriptions or evolutionary models.

Extreme physical processes are also expected in RSGs above a certain luminosity. Historically, the Humphreys-Davidson limit ($\log(L/L_{\odot}) = 5.8 \pm 0.1$ dex; Humphreys & Davidson 1979) empirically defines the RSG luminosity where instabilities presumably lead to large mass ejections (Glatzel & Kiriakidis 1993). Studies of RSGs in M31, the Large and Small Magellanic Cloud (LMC and SMC, respectively) have proposed a metallicity-independent limit at $\log(L/L_{\odot}) \sim 5.5$ dex (Davies & Beasor 2020; McDonald et al. 2022). Nevertheless, other recent works have found hints of RSGs with $\log(L/L_{\odot}) > 5.5$ dex in nearby galaxies (Antoniadis et al. 2024; de Wit et al. 2024, Maravelias et al., in prep.). The connection between stellar evolution and this empirical limit, as well as the physical processes therein, the

luminosity at which they occur, and the role of metallicity, are still poorly understood. Additionally, although RSGs are known to be the progenitors of Type II SNe (e.g., Heger et al. 2003; Smartt 2009; Langer 2012), the lack of observed explosions from the most massive ($M_{\text{ini}} > 18 M_{\odot}$) and luminous RSGs (i.e. the ‘RSG problem’; Smartt 2015) suggest that either they do not explode or evolve to warmer temperatures before exploding. Some studies, however, have argued that the ‘RSG problem’ may not be statistically significant (Davies & Beasor 2020; Beasor et al. 2024). The hypothesis that YHG are post-RSG objects and their typical luminosities ($\log(L/L_{\odot}) > 5.3$ dex, e.g., Kourniotis et al. 2017, 2022; Humphreys et al. 2023) suggest that they are the evolutionary products of the luminous RSG missing as Type-II SNe progenitors (Georgy 2012), potentially solving the problem.

Binary interactions add further complexity to the evolutionary picture of extreme RSGs. Since $\sim 90\%$ of massive stars are born in multiple systems (e.g. Sana et al. 2014; Bordier et al. 2022) and only $\sim 20\%$ of RSGs have detected companions (Neugent et al. 2020; Patrick et al. 2022), a considerable number of currently single RSGs might be unresolved binaries, have experienced binary interactions, a common envelope phase, a merger, or the death of their companion (Bonnell & Bate 2005; Sana et al. 2012). Binary interactions have been proposed to cause episodic mass ejections in apparent single RSGs such as Betelgeuse or VY CMa (Landri & Pejcha 2024; MacLeod et al. 2024). Therefore, the role of binarity in triggering episodic mass loss remains an open question from both observational and theoretical perspectives.

WOH G64 (IRAS 04553-6825, Westerlund et al. 1981) stands out as the most extreme RSG in the LMC, on the brink of the luminosity limit, ($\log(L/L_{\odot}) = 5.45$ dex, Ohnaka et al. 2008), being one of the coolest (M5-7.5e, Elias et al. 1986; Levesque et al. 2009), and the record-holder in terms of mass-loss rate ($\dot{M} > 10^{-4} M_{\odot} \text{ yr}^{-1}$; Beasor & Smith 2022; Antoniadis et al. 2024). Interferometric observations in the near and mid-IR revealed elongated emission, which was attributed to a dusty disk-like structure with a gaseous envelope of 3-9 M_{\odot} (Ohnaka et al. 2008, 2024). It is also an OH/IR star with strong multi-component maser emission possibly due to an external disk, two expanding dust shells, or bipolar outflows (van Loon et al. 2001; Marshall et al. 2004). This behavior closely parallels the Galactic RSG NML Cyg, which exhibits similar maser properties (Richards et al. 1996), leading researchers to propose WOH G64 as its LMC counterpart (Elias et al. 1986; van Loon et al. 2001).

In this study, we report the discovery of the dramatic transition of WOH G64, which exhibited the most extreme change in the optical spectrum ever seen in a RSG, from late-M to a B[e] star. In Section 2, we describe both the new observations obtained and the archival photometry and spectroscopy used. In Section 3, we report the observational changes of this object. Finally, in Section 4, we discuss the results and suggest scenarios for the dramatic transition, and summarize our work in Section 5.

2. Observations and data reduction

We obtained a new spectroscopic observation, which revealed the dramatic transition, and collected photometric and spectroscopic archival data of WOH G64 to investigate its nature. We describe the data in the following subsections.

2.1. Photometric catalogs

We assembled the photometry of WOH G64 available over the past decades from: ATLAS (Tonry et al. 2018), Gaia DR3 (Gaia Collaboration et al. 2016, 2023), the MACHO project (Alcock et al. 1997), NEOWISE (Mainzer et al. 2011), OGLE (Udalski et al. 1997, 2008, 2015), and WISE (Wright et al. 2010; Cutri et al. 2021). We applied the following criteria to each survey to select the most reliable data.

- ATLAS: We chose the reduced images option in the forced photometry server to obtain the light curve (Heinze et al. 2018; Shingles et al. 2021). We used data points with flag $err = 0$, $chi/N < 100$, and error lower than 0.2 mag. We binned the measurements within the same night to decrease the scatter.
- MACHO: We used the approximation $X \approx X_{Mt} + z_0 + 2.5 \log(ET)$ of Eq. 1 and 2 in Alcock et al. (1999) to produce the V_{KC} and R_{KC} photometry. In our approximation, X refers to the V_{KC} and R_{KC} bands, z_0 is the corresponding photometric zero point, and ET is the exposure time. We keep measurements with errors lower than 0.1 mag and discard outliers with small errors by applying a 3σ clipping.
- NEOWISE: WOH G64 has been observed on 21 main epochs since the mission started in 2014. We binned the measurements within each epoch by taking the median value and the uncertainty of the median. We discarded the data with $qual_frame = 0$ and $chi^2 > 20$. However, NEOWISE photometry differs from ALLWISE for targets brighter than $W1 < 8$ mag. We applied an offset according to Fig. 6 in Mainzer et al. (2014) to approximately correct the magnitudes. We discarded W2 because of saturation issues.
- OGLE: We used the V and I-band data from OGLE-III and OGLE-IV databases.

2.2. Spectroscopy

We obtained optical spectroscopy of WOH G64 with the Magellan Echelle (MagE) spectrograph (Marshall et al. 2008) on the 6.5-m Baade telescope at Las Campanas Observatory, Chile. We used the $1.0'' \times 10''$ long-slit, providing a wavelength coverage of 3500 – 9500 Å, a spectral resolution of $R \sim 4000$, and a spatial resolution of $0.3'' \text{ px}^{-1}$ with binning 1×1 . We used the MagE pipeline (Kelson et al. 2000; Kelson 2003) for the bias and flat correction. We manually continued the reduction using the ECHELLE package of IRAF¹. Finally, we used the flux standard to calibrate the spectrum with the IRAF routines STANDARD and SENSFUNC.

We further collected two spectra from the ESO archive, obtained with the instruments UVES (Dekker et al. 2000) and X-Shooter (Vernet et al. 2011) on the UT2 at the Very Large Telescope, Cerro Paranal, Chile. The UVES observations took place under the program ID 080.D-0508(A) (PI: A. Manchado). Two long exposures of 1800 s and a short of 300 s were obtained with the Cross Disperser #4, covering the spectral range 5655 – 9612 Å providing a spectral resolution $R \sim 57000$. The public data are not flux calibrated and were reduced using the official UVES pipeline v5.10.13 (Ballester et al. 2000). The X-Shooter spectra were obtained on the program ID 097.D-0605 (PI: S. Goldman) with the echelle slit spectroscopy mode. The $1.3''$ slit was used for the UVB arm, providing $R \sim 4100$,

¹ IRAF is distributed by the National Optical Astronomy Observatory, operated by the Association of Universities for Research in Astronomy (AURA) under agreement with the National Science Foundation.

Table 1: Log of spectroscopic observations

Telescope	Instrument	UT Date	Exp. time (s)	Slit width ($''$)
UT2 VLT 8m	UVES	2007 Oct 28	$2 \times 1800 + 1 \times 300$	0.7
UT2 VLT 8m	X-Shooter	2016 July 27	624 ^a , 980 ^{b,c}	1.2 ^{a,c} , 1.3 ^b
Magellan 6.5m	MagE	2021 Dec 17	$3 \times 180 + 1 \times 240$	1.0

Notes. ^aVis, ^bUVB, ^cNIR

while the 1.2 $''$ slit was used for the Vis and NIR arms, yielding $R \sim 6500$ and $R \sim 4300$ respectively. The spectral coverage was 2989 – 5560 Å, 5336 – 10200 Å, and 0.99 – 2.48 μm for the UVB, VIS, and NIR arms. Four images were combined to produce the final spectrum, with a total integration time per pixel of 980s in the UVB and NIR arms, and 624s in the VIS arm. The data were reduced with the official X-Shooter pipeline v2.7.0b (Modigliani et al. 2010). We corrected the final NIR spectrum for telluric absorption with MOLECFIT (v4.3.1, Smette et al. 2015), which calculates a synthetic spectrum of the Earth’s atmosphere based on local weather conditions and standard atmospheric profiles. X-Shooter is a supported instrument by MOLECFIT, hence we used the default parameters set up in the workflow. However, we refined the spectral regions considered for the telluric correction to optimize the cleaning in the J , H , and K bands.

The log of the spectroscopic observations, listing the telescope, instrument, UT date of the observation, exposure time, and the slit width is shown in Table 1.

3. Results

3.1. Optical light curve

We construct the light curve of WOH G64, ranging from 1992 until the submission date of this work, using the data described in Sect. 2.1. We clearly distinguish two different trends within the light curve (Fig. 1):

- From 1992 to 2014, WOH G64 exhibits a semi-regular periodicity of ~ 900 d with an amplitude of $\Delta V \sim 2$ mag and $\Delta I \sim 1.5$ mag. The OGLE-III survey (Soszynski et al. 2009) classified WOH G64 as a Mira variable based on its photometric variability. Moreover, Groenewegen et al. (2009) derived a fundamental period $P = 855.79 \pm 0.03$ d with $\Delta R_{\text{KC}} = 0.68$ mag and a long secondary period (LSP) of 2647 ± 1 d with $\Delta R_{\text{KC}} = 0.26$ mag from MACHO R_{KC} , while Groenewegen et al. (2020) obtained $P = 886$ d with $\Delta I = 1$ mag and a LSP of 3788 d with $\Delta I = 0.4$ mag from OGLE-III I -band.
- After 2014, the major semi-regular periodicity has vanished and irregular variability dominates the light curve. The star had almost constant brightness for 1 yr after 2015 and gradually increased by $\Delta I = 0.7$ mag between 2016 and 2019. Since then, its brightness has decreased $\Delta I = 1.6$ mag, except for one brightening of $\Delta I \approx 0.3$ mag lasting for a month. Since the peak of the small outburst in January 2024, the star decreased by $\Delta o \approx 2$ mag in 10 months. The lack of data between early 2020 and the beginning of 2022 prevents reporting if there was another small outburst, as suggested by the mid-IR light curve (see Sect. 3.2).

Apart from the main variability, we found low-amplitude, $\Delta V \sim 0.1$ mag, sinusoidal variations lasting 20–40 d, which remain present along the entire light curve. Inspired by the 12.4 d

low-amplitude sinusoidal variability of the SN 2022jli due to a compact companion (Moore et al. 2023; Chen et al. 2024), we tried to analyze its periodicity without any successful results. In Fig. 2 we present the colors $V - I$ and $BP - RP$ with time to illustrate the evolution of the system. We detect a significant transition of $\Delta(V - I) \approx 1.8$ mag to a bluer color between mid-2013 and mid-2014. This major color change is exclusively due to the abrupt change of the V -band within a year, while the I -band remained almost constant. The lack of measurements in the V -band during this time prevents us from constraining the exact time of the transition. The color and the variability changes match in time with the extreme transition in the spectral features observed through optical spectroscopy (see Sect. 3.3). Before 2014, WOH G64 was classified as a late M-type RSG, had a Mira-like variability, and a very red color, $V - I \approx 5$ mag. However, after 2015, the star lost its periodicity, had a bluer color ($V - I \approx 3.2$ mag), and exhibited spectral emission features typically seen in B[e]-stars.

3.2. Mid-infrared light curve

We investigate the mid-IR variability of WOH G64 using W1 from NEOWISE (Fig. 3). The start of the mission around 2014 coincides with the time when WOH G64 experienced the transition (see Sect. 3.1 & 3.3). Nevertheless, we do not see any major variation with respect to the epoch from WISE in 2010, before the transition. The W1 photometry shows three outbursts of $\Delta W1 \sim 1$ mag, but outside these is approximately constant at $W1 = 5.4$ mag with a standard deviation of $\Delta W1 = 0.1$ mag, which is smaller than the error. The outbursts had an amplitude $\Delta W1 \approx 1$ mag in mid-2019, mid-2021, and mid-2023 (MJD=58631, 59359, and 60094, respectively), showing a potential ~ 750 d recurrence. The low cadence of NEOWISE prevents us from determining when exactly the peaks occurred. Interestingly, the first mid-IR outburst coincided with a peak in the optical light curve. The second mid-IR peak occurred during a gap in the optical photometry, while the third peak had a delayed optical counterpart. These outbursts are reminiscent of bumper events of Be stars (Kourniotis et al. 2014), which are related to the build-up and decay of their decretion disks and have been observed in the mid-IR to have amplitudes up to 1.5 mag (Jian et al. 2024). Finally, we calculated the median absolute deviation (MAD) of the NEOWISE data, a robust indicator to assess variability (Sokolovsky et al. 2017), finding $\text{MAD}_{W1} = 0.158$. This large value exceeds the MAD_{W1} values of all RSGs in the LMC (Antoniadis et al. 2024), although WOH G64 was classified as a B[e] star when the mid-IR data were obtained.

3.3. Optical spectroscopy

WOH G64 is a well-studied extreme RSG that has been spectroscopically classified as late M-type in several works since the

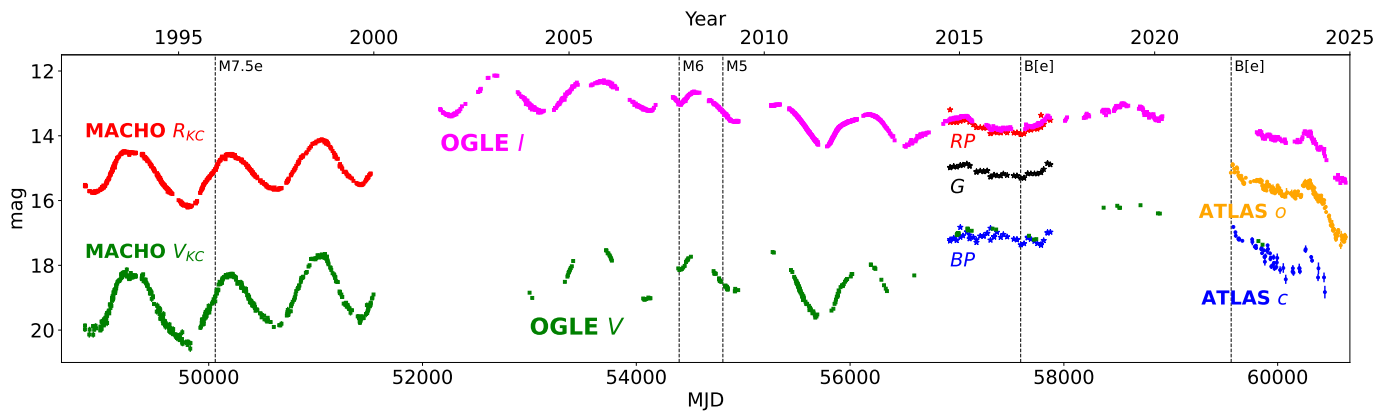


Fig. 1: Optical light curves of WOH G64 spanning >30 years. The vertical lines indicate the spectroscopic epochs presented in Table 2.

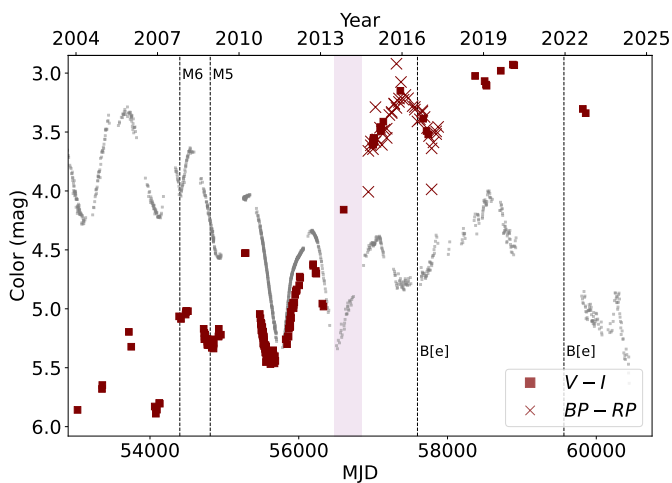


Fig. 2: Evolution of the optical colors OGLE $V - I$ (squares) and *Gaia* $BP - RP$ (crosses). OGLE I -band (grey points) is shown with an offset for comparison. Vertical dashed lines indicate the optical spectral classifications from Table 2. The estimated time of the transition between 2013.5 and 2014.5 is highlighted with the shaded area.

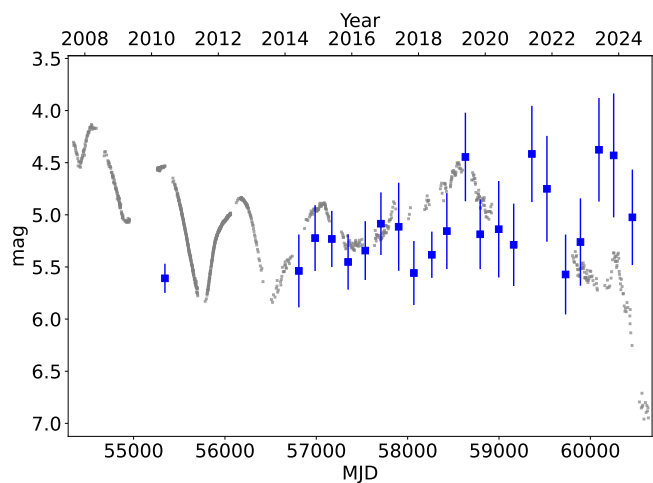


Fig. 3: Mid-IR light curve of W1 (blue squares) from ALLWISE and NEOWISE. The OGLE I -band (grey squares) is shown with an offset for comparison.

Table 2: Optical spectral classifications of WOH G64

Reference	UT Date	Spectral Class.
Elias et al. (1986)	–	M7.5
van Loon et al. (2005)	1995 Dec 8-11	M5-7.5e
This work	2007 Oct 28	M6
Levesque et al. (2009)	2008 Dec 10	M5
This work	2016 Jul 27	B[e] star
This work	2021 Dec 17	B[e] star

1980s (see Table 2). These studies also reported nebular emission from $H\alpha$, $H\beta$, $[N\ II]$, $[O\ I]$, $[O\ III]$, and $[S\ II]$.

The unpublished UVES spectrum from 2007 (Sect. 2.2) exhibits features characteristic of late M-type RSGs, such as deep TiO bands, strong Ca II triplet, and absorption lines from Fe I, Mg I and Ti I (Fig. 4 & 5). Strangely, the Mg I lines at $\lambda\lambda 8500$ – 8800 (Tabernero et al. 2018) are absent. We followed the spectral classification of Solf (1978) based on the strength of TiO and VO bands. The existence of the heads of TiO at $\lambda\lambda 8199$, 8420, 8506, 8515 suggests that its spectral type is M5 or later. We classify it as an M6 star because of the existence of TiO at $\lambda\lambda 8206$, 8251, 8268, 8373, and 8420 and the strength of the TiO bands at $\lambda\lambda 8432$, 8442 compared to the Ca II lines. We only identify the VO head at $\lambda 7865$ out of the two that start to appear at M6 ($\lambda\lambda 7865$, 7897). We also detect emission from $H\alpha$ as well as forbidden lines, such as $[N\ I]$ $\lambda 5198$, $[N\ II]$ $\lambda\lambda 6548$ and 6583, $[S\ II]$ $\lambda\lambda 6716$ and 6731, $[O\ I]$ $\lambda\lambda 6300$ and 6364. We highlight the double-peaked $[N\ II]$ and $[S\ II]$ emission, with their components separated by $\sim 210\text{ km s}^{-1}$ and $\sim 100\text{ km s}^{-1}$, respectively (see Appendix A).

Nevertheless, the X-shooter spectrum from 2016 reveals dramatic changes. The TiO bands have completely disappeared, and double-peaked and asymmetric emission lines dominate the spectrum. The only absorption lines in the optical range are K I $\lambda\lambda 7665$ and 7699, and Na I $\lambda\lambda 5890$ and 5896. The forbidden transitions found are from $[Fe\ II]$, $[N\ I]$ $\lambda\lambda 5198$, 10398 and 10407, $[N\ II]$ $\lambda\lambda 6548$ and 6583, $[S\ II]$ $\lambda\lambda 6716$ and 6731, $[O\ I]$ $\lambda\lambda 6300$ and 6364 and $[Ca\ II]$ $\lambda\lambda 7291$ and 7324, while the majority of permitted transitions arise from Fe I, Fe II, Ni I and Ti I. Additionally, the Ca II triplet and $H\alpha$ are double-peaked, while the Paschen series and He I $\lambda 6678$ show asymmetric emission.

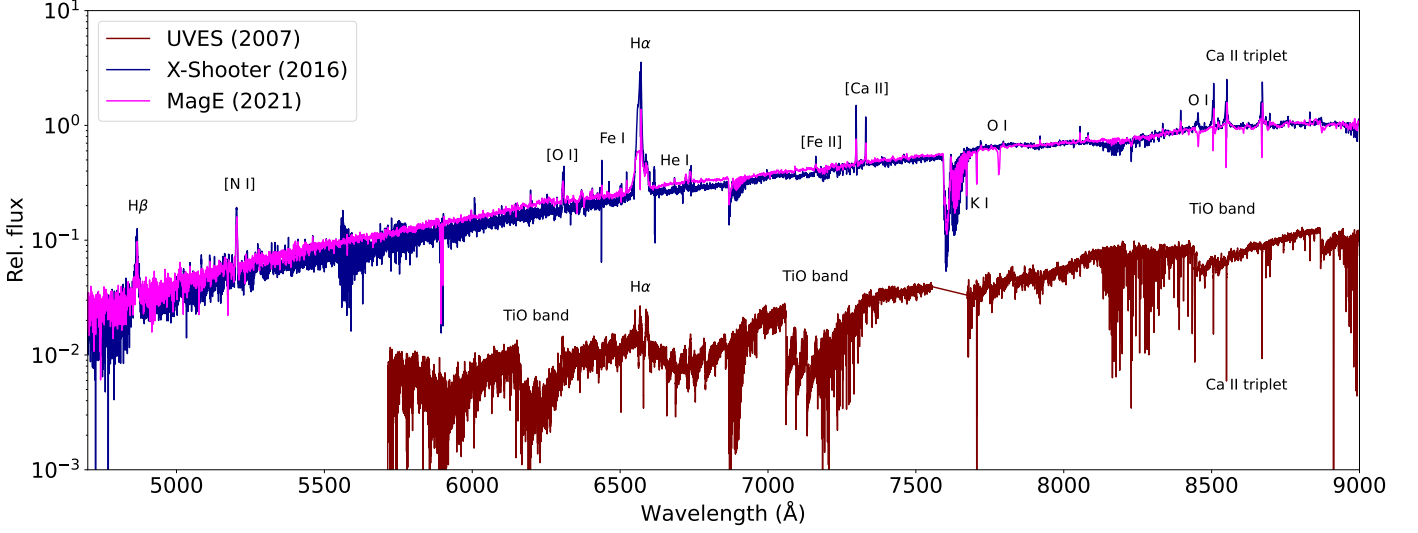


Fig. 4: Optical spectra of WOH G64 from UVES, X-Shooter, and MagE, highlighting the main spectral features and their evolution with time.

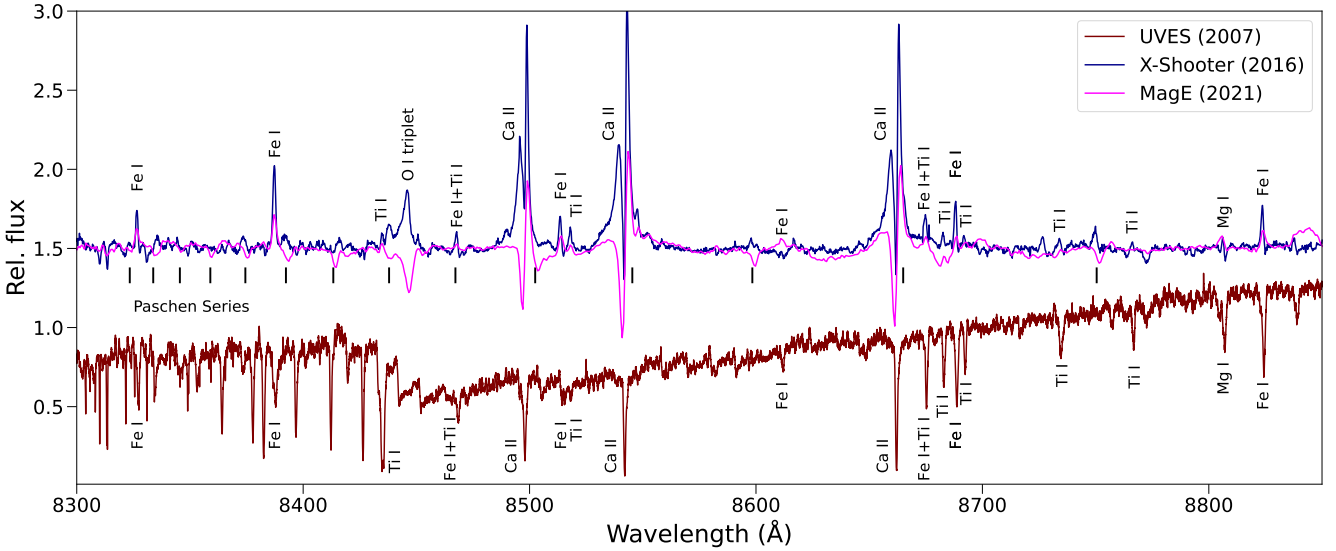


Fig. 5: Same as Fig. 4, but for the Ca II triplet spectral region.

Notably, the O I triplet $\lambda 8446$ is in emission, while the O I triplet $\lambda 7774$ is barely in absorption.

The MagE spectrum obtained in 2021 reveals various changes with respect to 2016. The asymmetric and double-peak emission lines still dominate the optical range, but new absorption lines emerged. Along with the K I and Na I, Si II $\lambda\lambda 6347$ and 6371 , Sc II series at $\lambda\lambda 5500$ - 5700 , the O I triplets $\lambda\lambda 8446$ and 7774 , and Paschen series also appear in absorption. Moreover, H α and the Ca II triplet have P Cygni profiles, rather than the double-peaked emission in 2016. We measured the outflow velocities in H α and the Ca II triplet from the minima in their P Cygni profiles relative to the emission line peak, finding 80 ± 10 and 90 ± 10 km s $^{-1}$, respectively. These outflow velocities are lower than those typically found in the Luminous Blue Variable, Warm Hypergiants, and other Supergiants in M33 and M31 (Humphreys et al. 2014). The change from double-peaked to P Cygni profiles in the Ca II, and from emission to absorption in the O I triplets and the Paschen series might indicate deceler-

ation of the stellar wind. Nevertheless, the emission of permitted transition from Fe I, Fe II, Ni I, and Ti I and the forbidden transition from [Fe II], [N I] $\lambda 5198$, [N II] $\lambda\lambda 6548$ and 6583 , [S II] $\lambda\lambda 6716$ and 6731 , [O I] $\lambda\lambda 6300$ and 6364 and [Ca II] $\lambda\lambda 7291$ and 7324 remain.

We dedicate Appendix A to discuss the forbidden emission lines, list the lines found in the optical regime in Table B.1, and show regions of the X-Shooter and MagE spectra in detail in Appendix C. The emission from [Ca II], Fe I, Fe II, [Fe II], [O I] and the Balmer series, and the very weak He I, lead to a B[e] star classification. We classify the new state as a B[e] star, instead of supergiant B[e] (sgB[e]), to be conservative (see Sec. 4.1) as various systems with different nature can show the B[e] phenomenon (Lamers et al. 1998). The lines detected in WOH G64 match exactly with J004415.00+420156.2 and J013426.11+303424.7, two Fe II emission line stars, reclassified as sgB[e] stars (Humphreys et al. 2014, 2017).

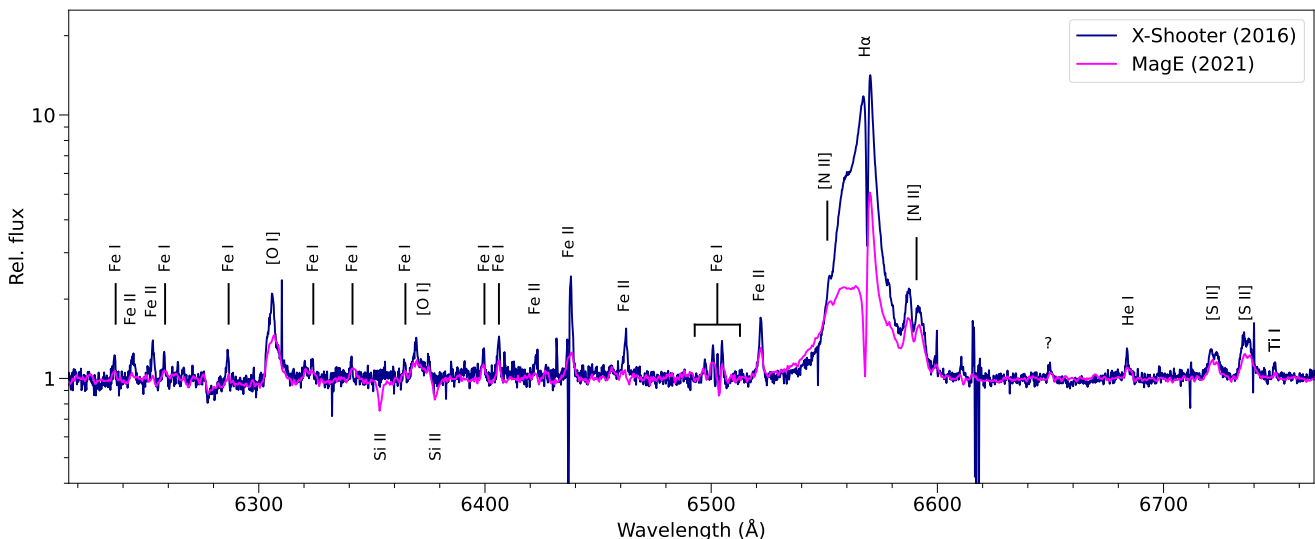


Fig. 6: Comparison of the $H\alpha$ spectral region of the optical spectra of WOH G64 from X-Shooter and MagE, highlighting the main absorption and emission lines and their evolution with time.

3.4. Near-infrared spectroscopy

We show the telluric-cleaned spectrum obtained with the NIR arm of X-Shooter in Fig. D.1, covering the bands YJ (1.0–1.35 μm), H (1.4–1.75 μm) and K (2.02–2.45 μm). We report the main spectral lines in Table B.2. The strong asymmetric emission from the Paschen series and the He I triplet at 1.083 μm dominate the spectrum in the YJ -band. We identified various emission series from Ti I at 1.03–1.08 μm and 1.26–1.31 μm and Fe I at 1.16–1.20 μm . We also report the presence of the forbidden multiplet of [N I] at 1.04 μm , and several absorption lines of Si I. We note the absence of the Mg I lines typically found at 1.16–1.20 μm (Bergemann et al. 2015), which might be filled with emission. In contrast to the optical range and the J -band, the H -band is completely dominated by absorption lines without any clear emission lines standing out. We indicate in Fig. D.1 the location of three Ti I atomic lines, with similar energy levels as those reported in the J -band, which are embedded within the absorption lines. In the K -band, we report strong asymmetric emission from Br γ , a series of Ti I, and several unidentified emission lines. The spectral range 2.25–2.45 μm is usually dominated by CO-bands in sgB[e] and cool stars. However, we do not detect well-defined CO-bands, only broad features that might be reduction artifacts, hence we do not consider them further.

We used the absorption lines in the H -band to constrain the spectral type of WOH G64 in 2016 based on the near-IR atlas from Rayner et al. (2009). The lack of the Br series indicates a late-G type or later. We do not see molecular CO features nor the bump due to H^- opacity, which both appear in late K-types. Therefore, we conclude that WOH G64 has a late-G or early-K spectral type. We also used APOGEE DR17 (Abdurro'uf et al. 2022) to compare WOH G64 with the H -band spectra of four stars from the LMC to constrain the T_{eff} . We chose: LHA 120-S 89, the sgB[e] from Kraus (2019) with the most similar luminosity to WOH G64; [W60] B90, an M-type extreme RSG undergoing episodic mass loss (de Wit et al. 2023; Munoz-Sanchez et al. 2024), and two warm stars with the highest S/N with $\log(g) < 1$ dex and $4500 < T_{\text{eff}} < 5000$ K. We selected this T_{eff} range because the He I lines become stronger at warmer T_{eff} and are not present in WOH G64. The two warm stars are [MA93] 897, a RSG with a hot companion (Patrick

et al. 2022), and HV 2251, a yellow supergiant candidate (Neugent et al. 2012) and a classical Cepheid based on its variability (Soszynski et al. 2009). We compare WOH G64 with the four selected stars in Fig. 7, highlighting the T_{eff} reported in APOGEE. Despite the B[e] features found in the optical regime, this spectral classification is incompatible with the H -band. Moreover, WOH G64 does not show the same RSG features as [W60] B90, indicating a warmer T_{eff} . However, HV 2251 and [MA93] 897 are similar to WOH G64. We therefore estimate $T_{\text{eff}} \sim 4700$ K for WOH G64, which agrees with the late-G and early-K classification and the lack of TiO bands in the optical range. However, it cannot explain the He I emission in the optical and the J -band, hinting at a potential composite spectrum as the result of a binary system (see Sect. 4.1.2).

3.5. Radial velocity

We measured the heliocentric radial velocity (RV) from the emission and absorption lines for the three different epochs with the `splot` package of IRAF. We highlight the RV measurements from the most relevant emission lines from permitted transitions in Table 3. The H -band absorption lines from the X-Shooter spectrum were measured by cross-correlating it with the atomic features from a MARCS model with $T_{\text{eff}} = 4500$ K and $\log(g) = 0.0$ dex. Generally, the asymmetric emission profiles prevented the accurate determination of the center of the emission, enlarging the error. We excluded the Na I D lines from the analysis because they may be affected by circumstellar absorption and not indicate the stellar velocity.

The Ca II triplet is usually a good tracer for RV velocity changes in stars. However, its asymmetric emission in 2016 and the P Cygni shape in 2021 prevented us from analyzing RV variations through our epochs. We report 285 ± 2 km s $^{-1}$ from the UVES spectrum, which is in agreement with 292 ± 15 km s $^{-1}$ from Levesque et al. (2009) and ~ 300 km s $^{-1}$ from van Loon et al. (1998). The UVES spectrum and the one presented in van Loon et al. (1998) have a similar spectral resolution, but a difference of 15 km s $^{-1}$ is not significant considering their rough RV estimation. These RV differences among epochs could be associ-

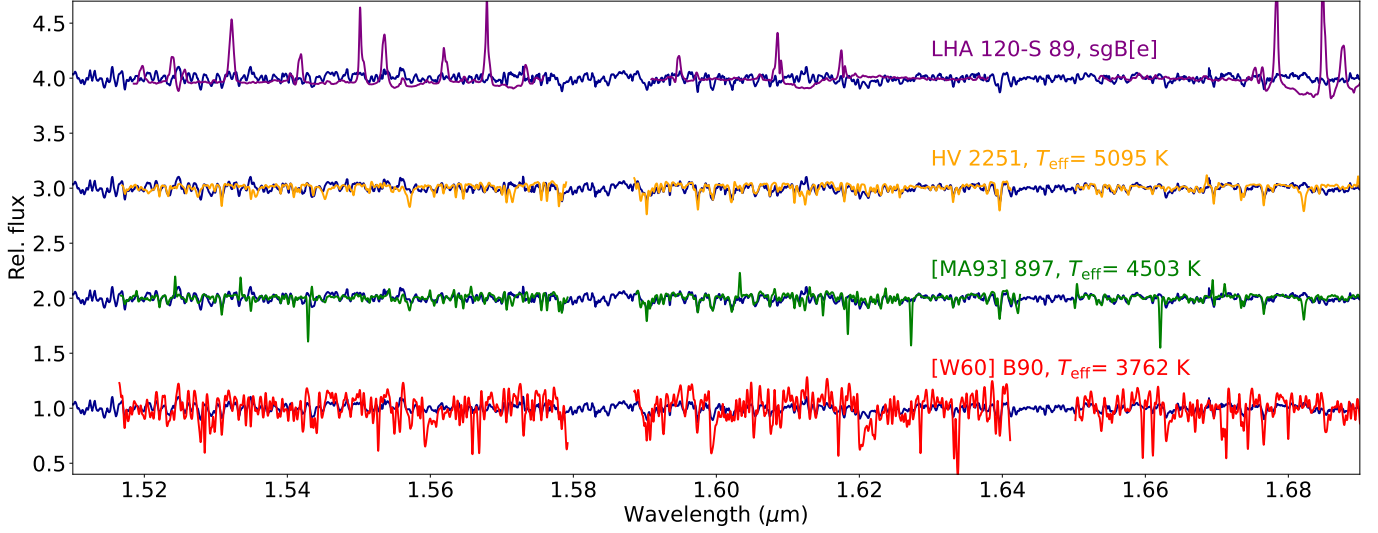


Fig. 7: Comparison of the H-band of WOH G64 from X-Shooter (blue) in 2016 with the APOGEE spectra of four supergiants of the LMC, indicating their T_{eff} reported in APOGEE.

ated with atmospheric convection, which can stochastically shift the lines by $\sim 10 \text{ km s}^{-1}$ (Kravchenko et al. 2019, 2021).

The RV is consistent within errors at $\sim 290 \text{ km s}^{-1}$ in the UVES spectrum and $\sim 270 \text{ km s}^{-1}$ in the X-Shooter spectrum. However, the RV of the lines in the MagE spectrum follows two trends. The neutral atomic emissions, such as Fe I, Ti I, and Ni I, are centered at $\sim 275 \text{ km s}^{-1}$, similarly to the X-Shooter epoch, but the absorption from Sc II, Si II and the Paschen series indicate $\sim 315 \text{ km s}^{-1}$. The 40 km s^{-1} difference between these two groups is significant and hints at a binary scenario (see Sect. 4.1.2). The unique lines detected in the UVES, X-Shooter, and MagE spectra are from Fe I and Ti I. We detect a shift of $\sim 20 \text{ km s}^{-1}$ in the Fe I lines and $\sim 10 \text{ km s}^{-1}$ in Ti I between the absorption in the UVES spectrum with respect to emission in X-Shooter and MagE epochs, but the large errors prevent further analysis.

Table 3: Radial velocity in km s^{-1} of permitted lines

Lines	RV _{UVES}	RV _{X-Shooter}	RV _{MagE}
Ca II triplet	285 ± 2	—	—
Fe I	294 ± 9	$270 \pm 8^*$	$272 \pm 14^*$
Ti I	289 ± 5	$276 \pm 6^*$	$278 \pm 4^*$
Na I ($\lambda\lambda$ 8183, 8194)	288 ± 1	—	—
Ni I	—	$269 \pm 4^*$	$278 \pm 8^*$
Sc II	—	—	315 ± 7
Si II	—	—	305 ± 6
Paschen series	—	$269 \pm 6^*$	321 ± 7
Si I (J-band)	—	282 ± 4	—
H-band	—	269 ± 4	—
Na I D lines	255 ± 1	262 ± 2	245 ± 3

Notes. *RV measured from emission lines

4. Discussion

Numerous works have previously classified WOH G64 as a RSG based on its spectral features in the optical (Elias et al. 1986; van Loon et al. 1998; Levesque et al. 2009), in the near-IR (Ohnaka et al. 2024), its K-band variability (Wood et al. 1992), and the equivalent width of the Ca II triplet (van Loon et al. 1998). Moreover, its variability $\Delta V \sim 2 \text{ mag}$ in the optical (van Loon et al. 1998), its spectral energy distribution (Elias et al. 1986), and the multi-component maser emission from different outflows (van Loon et al. 1998, 2001; Marshall et al. 2004) resemble the properties seen in the Galactic RSG NML Cyg (Richards et al. 1996).

4.1. Spectral change

Since the transition in 2014, the optical spectral classification of WOH G64 has changed from a late-M to a B[e] star (see Sect. 3.1 and 3.3). The B[e] phenomenon encompasses stars with Balmer emission lines, low excitation permitted emission lines of low ionization metals in the optical spectrum, forbidden emission lines typically from [Fe II], [Ca II] and [O I] in the optical spectrum, and a strong near or mid-infrared excess due to hot circumstellar dust (Kraus 2019). In this section, we explore whether the B[e] phenomenon in WOH G64 arises from a sgB[e] or a symbiotic star, SymB[e] (Lamers et al. 1998).

4.1.1. Supergiant B[e] scenario

The B[e] features and the high luminosity of WOH G64, $\log(L/L_{\odot}) = 5.45 \text{ dex}$, are in agreement with a sgB[e] classification. However, a sgB[e] is incompatible with the yellow-star features in the H-band (Fig. 7). Furthermore, WOH G64 has undergone a decline of $\Delta I \approx 2 \text{ mag}$ since 2019, which does not agree characteristic photometric variability of sgB[e]s ($\Delta m \lesssim 0.5 \text{ mag}$, Lamers et al. 1998; Kraus 2019; Maravelias et al. 2023). The composite spectral features and the large variability rule out the sgB[e] scenario for WOH G64, although it may transition to a sgB[e] in the future (see Sect. 4.5).

4.1.2. Symbiotic B[e] scenario

SymbB[e] stars are interacting binaries, typically consisting of a cool giant and a hot companion (Lamers et al. 1998), such as a white dwarf (e.g., Mikołajewska 2003). However, several massive symbiotic analogs have been reported, such as Object X in M33, a binary composed of a massive O star and a dust-enshrouded red hypergiant (Khan et al. 2011; Mikołajewska et al. 2015), or J004032.98+404102.8 in M31, an RSG plus OB pair (Neugent et al. 2019). HR 5171 is also an interacting binary consisting of a YHG plus a B-star (Chesneau et al. 2014; van Genderen et al. 2015). The YHG in HR 5171, just as in WOH G64, is classified as a late-G or early-K, even though its optical spectrum lacks B[e] features. SymbB[e] stars typically show irregular variability and evidence of a cool star in the optical range, or a late-type stellar spectrum in the near-IR. WOH G64 displays both irregular variability since 2014 (see Sect. 3.1) and a composite spectrum, with yellow-star features in the *H*-band and B[e] features (e.g., He I, [Fe II]) in the optical (see Sect 3.3 and 3.4). Therefore, we propose WOH G64 to be a massive symbiotic binary exhibiting the B[e] phenomenon.

4.2. Further evidence for binarity

Several properties of WOH G64 are difficult to reconcile with a single star scenario, such as the composite spectral features (see Sect. 3.3 and 3.4), the RV changes (see Sect. 3.5), and the strong forbidden lines of [O I], [N II], and [S II] when it was a RSG (see Appendix A). Moreover, the existence of dense equatorial structures (e.g., the elliptical morphology in the *K*-band and the dusty torus; Ohnaka et al. 2008, 2024) provide further evidence for the binary scenario. Ohnaka et al. (2024) found that the mid-IR has persisted at 10 μm since 2004, indicating that the hot dust is confined to the central part of the system. A binary system could explain the confined dust, by keeping it bound within the orbit. Levesque et al. (2009) considered the binary scenario to explain the $\sim 50 \text{ km s}^{-1}$ shift between the nebular emission and the stellar features from the star, but finally proposed a scenario of scattering within the expanding dust shell.

The lack of an outburst during the transition rules out a violent event such as a merger or the explosion of the RSG. Therefore, we assume a binary scenario with two objects before and after the transition. Since the *I*-band does not dramatically change during the transition, we assume that the same object dominates the system after the spectral change. As the system currently consists of a warm and a hot star, we examine whether the previous RSG has evolved into a YHG or a BSG.

Assuming its evolution to a YHG, the SymbB[e] would be currently formed by a B-star and a YHG. According to stellar evolution and if the binary has a high mass ratio, WOH G64 could evolve until the last stages within the RSG phase and still have a B-star companion with a comparable luminosity to produce the He I lines detected. The orbit including a RSG and a B companion should be a few 2000 – 4000 d to avoid the companion from entering the RSG atmosphere. The observed binary fraction ($\sim 20 \%$) of RSGs with a hot companion in the LMC and SMC (Neugent et al. 2019, 2020; Patrick et al. 2022) supports the feasibility of such a scenario.

Alternatively, if WOH G64 evolved to a BSG, the system would consist of a BSG in a post-RSG phase and a yellow star. The yellow star must be a supergiant to be comparable in luminosity to the BSG and to dominate in the near-IR, as a yellow main-sequence star would be 10^5 times less luminous. Furthermore, the YSG companion should be in a pre-RSG phase, be-

cause it has to be less luminous and less evolved than WOH G64, as it was not previously detected. However, a pre-RSG YSG phase lasts only on the order of $\sim 10^4$ years for such high initial masses (Neugent et al. 2012). Having a system formed by a YSG and a BSG in a post-RSG phase is therefore very unlikely, as the two objects would be in instantaneous phases in terms of stellar evolution timescales. Moreover, the fast, yet smooth transition within a year and without an outburst from RSG to a YHG (from $T_{\text{eff}} \sim 3200 \text{ K}$ to $T_{\text{eff}} \sim 4700 \text{ K}$) is more likely, rather than changing to a BSG ($T_{\text{eff}} \gtrsim 20000 \text{ K}$). Therefore, we conclude that WOH G64 transitioned to a YHG.

4.3. Explaining the transition

We attributed the transition to the change from a very cool RSG to a YHG assuming the B-star companion is unaltered (see Sect. 4.1.2). Dimming events can temporarily change the spectral type of a RSG, as in HV 11423 (Massey et al. 2007) and [W60] B90 (Munoz-Sanchez et al. 2024). HV 11423, the coolest RSG in the SMC, changed from 3500 K to 4300 K in a year after a dimming event. However, the outstanding change in WOH G64 is persistent in time and the lack of variability in the *I*-band suggests a different physical process than a dimming event. The $\Delta V \sim 2 \text{ mag}$ increase and the *V* – *I* change can be attributed to the disappearance of the TiO bands and the ejection of the outer molecular layers. Interferometric observations in the *K*-band during December 2020, revealed an elliptical ring structure surrounding the star with a semi-minor axis of 3 mas (Ohnaka et al. 2024). We examine whether this ring could be the outer layer ejected causing the transition. Assuming 90 km s^{-1} from the outflow velocity measured from the P Cygni emission lines of the Ca II triplet, an ejected layer would need around 7.7 yr to be at 3 mas from the star. This timescale would correspond with an ejection of the layer during March 2013, approximately some months before the start of the transition. This timescale hints at this ring as the ejected outer part of the envelope. Nevertheless, repeating the *K*-band interferometry of WOH G64 under the same conditions as in Ohnaka et al. (2024) would be necessary to confirm the expansion velocity of the ring, and to determine whether it is a stationary structure or an artifact of the image reconstruction process.

WOH G64 may be a post-RSG object evolving towards warmer temperatures by losing outer part of its envelope. Below, we explore several scenarios to explain the transition.

4.3.1. Superwind phase

Very luminous RSGs with $\dot{M} \sim 10^{-4} M_{\odot} \text{ yr}^{-1}$ (e.g. Yang et al. 2023) naturally evolve to a YHG phase before ending their lives (see the effect of Yang+23 winds in Zapartas et al. 2024). However, the timescale of such evolution is larger than the observed in WOH G64. The disappearance of the semi-regular variability during the transition to YHG might be the key to explaining the physical processes therein. The semi-regular variability in RSGs is linked to pulsations with periods between 300-1000 days and $\Delta V < 1 \text{ mag}$ (Chatys et al. 2019). However, the $\Delta V \sim 2 \text{ mag}$ variability of WOH G64 suggests an abnormally strong pulsation. Heger et al. (1997) proposed that RSGs with high luminosity-mass relation may exhibit large-amplitude pulsations, preferentially as OH/IR sources, and experience a superwind of $\dot{M} \sim 10^{-4} M_{\odot} \text{ yr}^{-1}$ during the last thousand years before the SN explosion. WOH G64 is a well-known OH/IR source (e.g., Wood et al. 1992) and the superwind theory coin-

cides with the high \dot{M} estimated for WOH G64 (Beasor & Smith 2022; Antoniadis et al. 2024). A superwind in a pre-SN phase might explain the evolution of WOH G64 to a warmer T_{eff} and the obscuration of the system due to high mass loss. WOH G64 might be the example of how the pre-SN superwind phase could drive the evolution of the most luminous RSGs to warmer temperatures, preventing their explosion as RSGs and contributing to the speculated 'RSG problem' (Smartt 2015). The pre-SN superwind phase in WOH G64 might indicate its explosion within the next hundred years. Pre-SN superwind theory is disfavored in Type IIP SN progenitors because the RSG would be obscured decades before the explosion, which contradicts the observations of progenitors within 10 yr before the SN explosion Davies et al. (2022). However, WOH G64 is not a RSG anymore and the new YHG state suggests that it would explode as a Type IIb or Type III SN, rather than a Type IIP (see Sect. 4.5).

4.3.2. Binary interaction

Binary interactions could explain the massive envelope enshrouding WOH G64 if they are the dominant mechanism for the mass ejection. The high obscuration of WOH G64 ($A_V > 8$ mag, Beasor & Smith 2022) is created by a torus-shaped, dusty-gaseous envelope, with an estimated mass of 3-9 M_{\odot} (Ohnaka et al. 2008). This extreme obscuration entails a high IR excess, which leads to an abnormal estimation of $\dot{M} > 10^{-4} M_{\odot} \text{ yr}^{-1}$ compared to the assumed RSG winds (e.g., de Jager et al. 1988; van Loon et al. 2001; Beasor & Smith 2022; Antoniadis et al. 2024). However, if the total amount of dust was not solely produced by the wind, \dot{M} would be overestimated. Several works have already proposed binary companions in wide orbits, which might trigger episodic mass loss in RSGs (e.g., VY CMa and Betelgeuse; MacLeod et al. 2024; Landri & Pejcha 2024).

We investigate different types of binary interactions, such as common-envelope evolution, grazing-envelope evolution, and stable mass transfer, which could explain the material surrounding WOH G64 and its transition. We discard common-envelope evolution because it would have occurred during the expansion of WOH G64 while entering the RSG phase (e.g., Ivanova et al. 2013). If the transition was due to the onset of common-envelope evolution, the product would be a stripped star instead of YHG. Moreover, the blue star would be engulfed and invisible. However, stable mass transfer through Roche-lobe overflow might explain the high \dot{M} if the binary system had an initially wide orbit (e.g., Ercolino et al. 2024). Nevertheless, in wide orbit systems, the RSG is not predicted to evolve towards the blue. Also, the long timescale of stable mass transfer to drive the evolution is incompatible with the duration of the transition. Alternatively, in the grazing envelope evolution scenario (Soker 2015), although it is mostly considered for interactions between stars of more extreme mass ratio, a stellar companion grazes the envelope of a giant star by a spiral-in process. The interaction creates jets removing the outskirts of the supergiant envelope and preventing the formation of a common envelope. Grazing envelope evolution can last from tens to hundreds of years and may form a bipolar nebula and equatorial ring around the binary system. This scenario could explain the origin of the [N II] and [S II] from bipolar outflows when WOH G64 was a RSG, as well as the dense equatorial ring structures (e.g., the elongated shape in the K-band, and the disk-torus morphology required to explain the SED; Ohnaka et al. 2008, 2024).

4.3.3. Var A-like eruption

The high luminosity of WOH G64 ($\log(L/L_{\odot}) = 5.45$ dex; Ohnaka et al. 2008) places it near the Humphreys–Davidson limit ($\log(L/L_{\odot}) \sim 5.5 - 5.8$; Humphreys & Davidson 1979; Davies & Beasor 2020) where extreme physical processes associated with significant eruptions are expected (Glatzel & Kiriakidis 1993). Moreover, Cheng et al. (2024) proposed that eruptions up to $\dot{M} \sim 10^{-2} M_{\odot} \text{ yr}^{-1}$ can occur in supergiants between $10000 > T_{\text{eff}} > 3100$ K when the local super-Eddington luminosity exceeds the binding energy of the overlying envelope. These eruptions can lead to major changes in the structure of the star and its observed properties. In particular, Var A, one of the most luminous stars in M33 (Hubble & Sandage 1953), underwent an eruption over ~ 45 yr, exhibiting features of a late-M star due to its thick wind ($\dot{M} \sim 10^{-4} M_{\odot} \text{ yr}^{-1}$; Humphreys et al. 1987, 2006). When the eruption ended, Var A returned to its YHG state, exhibiting F-type features accompanied by both forbidden and permitted emission lines. The transition in the wind from an M-type pseudo-photosphere to a warmer F-type star was poorly constrained to occur in a time range of 1-5 yr. The SED of Var A also changed, decreasing its luminosity and its brightness in both the near and mid-IR (see Sect. 4.4).

Similarly to Var A, WOH G64 might be a YHG undergoing an eruption for more than 30 yr, until it returned to a quiescent state in 2014. We compare the transitions of WOH G64 and Var A in the Hertzsprung–Russell diagram in Fig. 8. We also added the LMC population of YHGs (Kourniotis et al. 2022; Humphreys et al. 2023), YSGs (Neugent et al. 2012), and RSGs (Antoniadis et al. 2024), and various extreme Galactic YHGs with significant transitions such as ρ Cas (Lobel et al. 2003; van Genderen et al. 2019), HR 8752 (Nieuwenhuijzen et al. 2012) and IRC+10420 (Oudmaijer et al. 1996; Nieuwenhuijzen & de Jager 2000) for comparison. We included the MIST evolutionary tracks with initial rotation $v = 0.4v_{\text{rot}}$ and $[\text{Fe}/\text{H}] = -0.25$ dex (Dotter 2016; Choi et al. 2016). For WOH G64, we assumed $\log(L/L_{\odot}) = 5.45$ dex (Ohnaka et al. 2008), a minimum $T_{\text{eff}} = 3200$ K (Levesque et al. 2009) and a new $T_{\text{eff}} \sim 4700$ K based on the near-IR (see Sect. 3.4). The new position of WOH G64 in the Hertzsprung–Russell diagram matches with the MIST track of $M_{\text{ini}} = 28 M_{\odot}$ instead of $M_{\text{ini}} = 25 M_{\odot}$ (e.g., Ohnaka et al. 2008) and implies a current radius of $R \sim 800 R_{\odot}$, considerably smaller than before ($R = 1540 R_{\odot}$; Levesque et al. 2007). We estimated the T_{eff} of Var A in Fig. 8 according to the optical spectral classification from M-type to late-F, even though the same lines that determine the F-type classification in Var A, are detected in WOH G64. However, only WOH G64 shows He I features. Hence, following the same approach of the optical spectral classification in WOH G64 to estimate the T_{eff} , the transition would be from 3200 K to ≥ 20000 K. Note that the luminosity of Var A was calculated based on its bolometric magnitude, leading to a possible overestimation as the asymmetric morphology of the circumstellar material was not taken into account. The luminosity of WOH G64 was carefully derived (Ohnaka et al. 2008), demonstrating an overestimation up to 0.3 dex when the asymmetric morphology is not considered. The outstanding change in the optical, the faster transition, and the larger obscuration in WOH G64 suggest a more extreme event than in Var A.

4.3.4. Brightening after a previous merger

WOH G64 shares several characteristics with V838 Monocerotis, a peculiar binary that underwent an immense stellar explosion in 2002, leaving behind an expanding cool supergiant, a

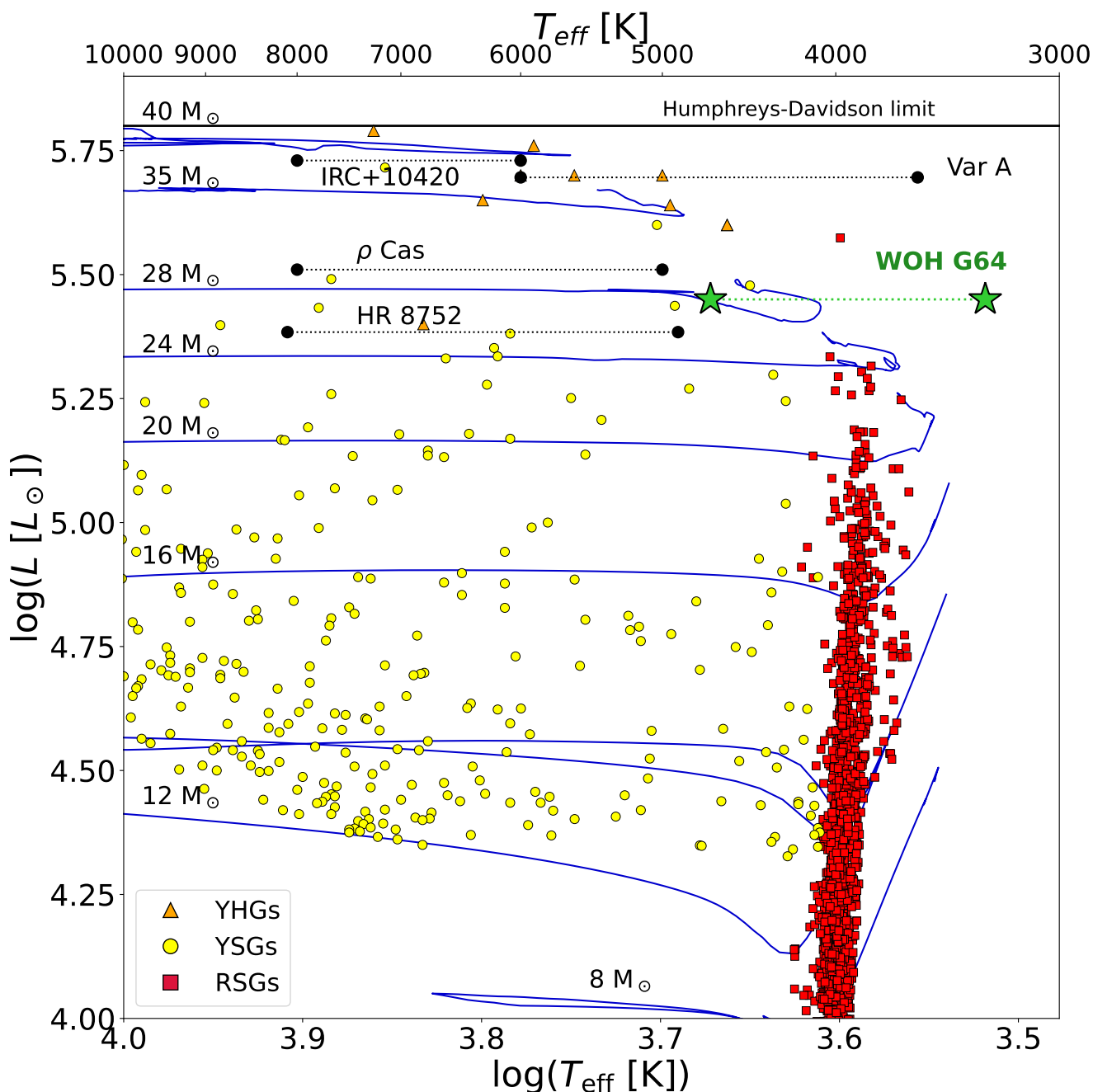


Fig. 8: Hertzsprung-Russell diagram showing the transition of WOH G64, compared to other extreme YHGs transitions (black dots) and the LMC population of YHGs (orange triangles, Kourmiotis et al. 2022; Humphreys et al. 2023), YSGs (yellow circles, Neugent et al. 2012), and RSGs (red squares, Antoniadis et al. 2024). MIST evolutionary tracks are presented in blue.

B3V companion, and a dense envelope of expanding molecular matter (Bond et al. 2003; Exter et al. 2016; Liimets et al. 2023). The most accepted explanation is a merger in a triple system causing a luminous red nova (Kamiński et al. 2021). Since then, the cool supergiant has been gradually brightening and increasing the temperature along 17 yr, changing from an L-type ($T_{\text{eff}} \sim 2300$ K, Evans et al. 2003) to a late-M ($T_{\text{eff}} \sim 3300$ K, Liimets et al. 2023). We explore whether WOH G64 could be an analog of V838 Monocerotis as they share the following characteristics: a very cool T_{eff} compared to other RSGs, a dense surrounding envelope, and a B-star companion. A merger should have occurred in a previous triple system during the last century

in WOH G64, expelling the material and obscuring the system. In this scenario, the transition could be similar to the brightening and increase in T_{eff} reported in V838 Monocerotis. We examined the APASS Catalog (B -band) within the Digital Access to a Sky Century at Harvard (DASCH; Grindlay et al. 2009) for detections of WOH G64 over the last century. If a merger occurred, the unobscured progenitors might have been detected in the B -band photometric plates. There are five detections with $16.0 < B < 17.2$ mag between 1928 and 1953 located at $9''$ from WOH G64. However, they might be associated with two stars within a $15''$ radius from WOH G64 with $B \sim 17$ mag (NO-

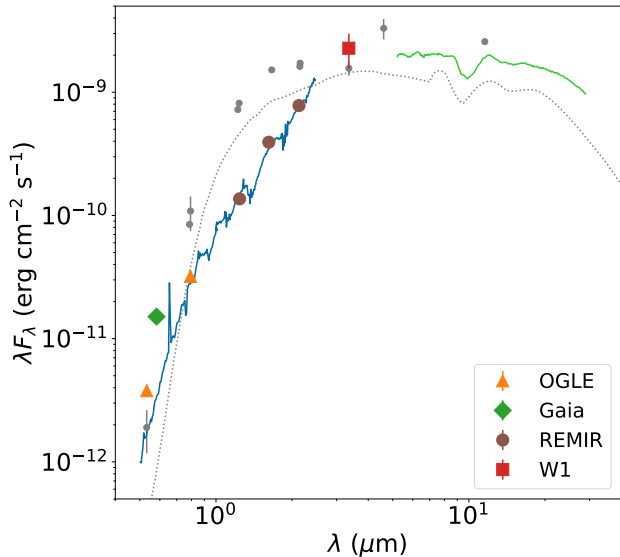


Fig. 9: SED of WOH G64 before (gray points) and after the transition (colored symbols), including the X-Shooter spectrum (blue) and the IRS spectrum (green, Houck et al. 2004). The dotted line is the best-fit model before the transition (Antoniadis et al. 2024).

MAD Catalog; Zacharias et al. 2004). Thus, we lack definitive evidence to support the merger hypothesis beyond speculation.

4.4. Spectral energy distribution

We investigated the differences in the spectral energy distribution (SED) of WOH G64 before (Antoniadis et al. 2024) and after the transition. We show this comparison in Fig. 9. We used the X-Shooter observations from July 2016 as a reference to construct the new SED. We collected OGLE V and I , W1, and G from the closest day to the X-Shooter observation (Sect 3.1 and 3.2). Ohnaka et al. (2024) demonstrated the constant shape at $10\ \mu\text{m}$ in the SED of WOH G64 since 2004. Hence we added the Spitzer InfraRed Spectrograph (IRS) Enhanced Product (Houck et al. 2004) as a reference in the mid-IR. We also used the JHK' photometry obtained by Ohnaka et al. (2024) in 2024 from the IR camera on the Rapid Eye Mount telescope (REMIR; Calzolari et al. 2005), as they found that it matches the SED of the X-Shooter spectrum.

The new SED reveals a dimming in the near-IR and a brightening in the V -band, consistent with a warmer T_{eff} after the transition. We find $\log(L/L_{\odot}) = 5.75 \pm 0.01$ dex before and $\log(L/L_{\odot}) = 5.57 \pm 0.01$ dex after the transition, by integrating the SED. We assumed spherical symmetry and a distance of 49.59 kpc (Pietrzyński et al. 2019). A similar decrease in the luminosity was reported in Var A, when it changed from an M-type to late-F (see Sect. 4.3.3). The apparent decrease in luminosity is possible in systems surrounded by a complex circumstellar environment as the radiation might escape from low-density regions, or even holes, in the obscuring material instead of the line-of-sight direction (Humphreys et al. 2006). Hence, we argue that the decrease in luminosity might be due to the complexity of the CSM around WOH G64, similar to that around Var A. Despite the change in luminosity, we adopt $\log(L/L_{\odot}) = 5.45$ from Ohnaka et al. (2008), as their luminosity calculation included spherical asymmetry.

4.5. Future evolution of WOH G64

The evolution of WOH G64 is difficult to predict, given our current understanding of the system. Between its two components, the YHG is the most evolved one, and therefore, is expected to end its life first, if both components evolve independently without significant interaction. The YHG is expected either to explode as a Type IIL SN, due to its partially stripped H-rich envelope or collapse into a black hole (e.g., Heger et al. 2003; O'Connor & Ott 2011). We note that lower-luminosity YSGs within interacting binary systems have been identified as progenitors of Type IIB SNe (e.g., SN1993J and SN2008ax; Van Dyk et al. 2002; Folatelli et al. 2015). Ultimately, the evolution of the YHG and its interaction with the B-star companion (see Sect 4.1.2) will determine the resulting Type IIL or Type IIB SN. The final explosion will potentially disrupt the rings and the envelope currently formed around WOH G64, leaving the B companion embedded in a SN remnant.

Alternatively, the YHG might implode into a black hole. A recent work reported the disappearance of a massive star in M31 with comparable properties ($\log(L/L_{\odot}) \sim 5.0$ dex and $T_{\text{eff}} \sim 4500$ K, De et al. 2024) to WOH G64. In a future similar scenario for WOH G64, the remaining B companion would appear as a single sgB[e], as the B[e] phenomenon and a disk-like structure are already observed (e.g., Ohnaka et al. 2008, 2024). Similarly to WOH G64, the Galactic YHGs HR 8752 and IRC+10420 (see Sect. 4.3.3) exhibit emission from [O I] and [Ca II] hinting at a Keplerian disk, resembling properties of sgB[e] and suggesting a sgB[e]-YHG connection (Aret et al. 2017; Klochkova 2019). Thus, studying the current state of WOH G64 and understanding the physical processes forming the equatorial disk structures may shed light on the formation of rings around sgB[e]s.

5. Summary

In this work, we report the dramatic transition of WOH G64, the most extreme RSG in the LMC. Since its discovery in 1986 (Elias et al. 1986), WOH G64 has exhibited spectral features of a very cool RSG with very deep TiO bands (see Table 2). However, our recent spectroscopic observations revealed a dramatic change in the optical (see Sect. 3.3). The X-Shooter archival optical spectrum from 2016 is completely dominated by asymmetric emission lines from permitted (e.g., Fe I, H I, He I, Ni I, and Ti I) and forbidden transitions (e.g., [Ca II], [Fe II], [N II], [O I], and [S II]) typically seen in B[e] stars (Lamers et al. 1998; Kraus 2019). Our MagE spectrum obtained in 2021 shows several absorption lines (e.g. Si II, Sc II and Paschen series) and the P Cygni emission of the Ca II showing outflow velocities of $90 \pm 10\ \text{km s}^{-1}$. The 30-yr optical light curve clearly shows two different trends that correlate with the dramatic spectral change (see Sect. 3.1). The transition occurred around 2014 when the star abruptly changed its $V - I$ color by 2 mag and ended its semi-regular variability. The W1 mid-IR light curve shows three outbursts of $\Delta W1 \sim 1$ mag since 2014 that have a possible recurrence of ~ 750 d (see Sect. 3.2).

We investigated the spectral change of WOH G64 from late-M to a B[e] star (see Sect. 4.1). The H -band in 2016 was dominated by atomic absorption lines indicating $T_{\text{eff}} \sim 4700$ K and being inconsistent with a sgB[e] classification (see Sect. 3.4). Additionally, the RV of the lines in the MagE spectrum follows two trends. The absorption lines from Sc II, Si II, and the Paschen series are $\sim 40\ \text{km s}^{-1}$ redshifted with respect to the rest of the lines (see Sect. 3.5). The discrepancy between the optical and the H -band, and the shifts in the RV favor a binary scenario and a

Symb[e] classification (Lamers et al. 1998). Therefore, we conclude that WOH G64 is a massive symbiotic system where the RSG has dramatically transitioned to a Yellow Hypergiant and, moreover, has a B-star companion (see Sect. 4.1.2).

We associate the loss of semi-regular variability, the null variation in the *I*-band, and the 2 mag brightening in the *V*-band to the disappearance of the TiO bands in its spectrum. The new parameters after the transitions align with the MIST track of $M_{\text{ini}} = 28 M_{\odot}$ and imply a new stellar size $R \sim 800 R_{\odot}$, in contrast to previous $R \sim 1500 R_{\odot}$ (Levesque et al. 2009). Interferometric observations in the *K*-band revealed an elliptical ring (Ohnaka et al. 2024), which could be the ejected outer envelope of the previous RSG. Assuming the outflow velocity from the Ca II triplet, the ejection of that ring should have occurred during March 2013, which is several months before the transition started. This result might probe the connection of that ring with the transition. We propose three possible scenarios: (a) WOH G64 was in a pre-SN superwind phase with $\dot{M} > 10^{-4} M_{\odot} \text{ yr}^{-1}$ and strong pulsations ejected the outer cool layers of the atmosphere (see Sect. 4.3.1), (b) a grazing envelope evolution disrupted the outer part of the atmosphere through binary interaction (see Sect. 4.3.2) or (c), similarly to Var A, WOH G64 was previously a YHG but in an outstanding eruption with a thick wind, creating a cool pseudo-atmosphere for more than 30 yr (see Sect. 4.3.3). The brightening from a previous merger (e.g. V838 Monocerotis; Bond et al. 2003; Exter et al. 2016; Liimets et al. 2023) was discarded (see Sect. 4.3.4). The new SED of WOH G64 has brightened in the optical and dimmed in the near-IR in agreement with the transition to a warmer T_{eff} (see Sect. 4.4). The current evolution of WOH G64 to a YHG before exploding provides a potential solution to the ‘RSG problem’ (Smartt 2015). The future binary interactions in the system will determine whether the YHG explodes as a Type III or Type IIb SN, or collapses into a black hole (see Sect. 4.5).

Monitoring WOH G64 is needed to study the future evolution of the components, unveil the properties of the proposed binary system, and clarify the cause of the transition. WOH G64 presents a unique opportunity to witness stellar evolution in real time and to understand the evolution of extreme RSGs and the physical processes occurring at high luminosity close to the Humphreys-Davidson limit.

Acknowledgements. GMS, MK, SdW, KA, AZB, EC and GM acknowledge funding support from the European Research Council (ERC) under the European Union’s Horizon 2020 research and innovation programme (“ASSESS”, Grant agreement No. 772086). EZ acknowledges support from the Hellenic Foundation for Research and Innovation (H.F.R.I.) under the “3rd Call for H.F.R.I. Research Projects to support Post-Doctoral Researchers” (Project No: 7933). This work has been co-funded by the National Science Centre, Poland, grant No. 2022/45/B/ST9/00243. We acknowledge helpful discussions with Michaela Kraus, Michalis Kournotis, Rene Oudmaijer, Lee Patrick, Ylva Göteborg, Andrea Ercolino, and Despina Hatzidimitriou. The work of KB is supported by NOIRLab, which is managed by the Association of Universities for Research in Astronomy (AURA) under a cooperative agreement with the U.S. National Science Foundation. This paper includes data gathered with the 6.5m Magellan Telescopes located at Las Campanas Observatory, Chile. Based on data obtained from the ESO Science Archive Facility with DOI(s): <https://doi.eso.org/10.18727/archive/71>. This work is based in part on observations made with the *Spitzer* Space Telescope, which is operated by the Jet Propulsion Laboratory, California Institute of Technology under a contract with NASA. This work has made use of data from the European Space Agency (ESA) mission *Gaia* (<https://www.cosmos.esa.int/gaia>), processed by the *Gaia* Data Processing and Analysis Consortium (DPAC, <https://www.cosmos.esa.int/web/gaia/dpac/consortium>). Funding for the DPAC has been provided by national institutions, in particular, the institutions participating in the *Gaia* Multilateral Agreement. This publication makes use of data products from the Near-Earth Object Wide-field Infrared Survey Explorer (NEOWISE), which is a joint project of the Jet Propulsion Laboratory/California

Institute of Technology and the University of Arizona. NEOWISE is funded by the National Aeronautics and Space Administration. This work has made use of data from the Asteroid Terrestrial-impact Last Alert System (ATLAS) project. The Asteroid Terrestrial-impact Last Alert System (ATLAS) project is primarily funded to search for near earth asteroids through NASA grants NN12AR55G, 80NSSC18K0284, and 80NSSC18K1575; byproducts of the NEO search include images and catalogs from the survey area. This work was partially funded by Kepler/K2 grant J1944/80NSSC19K0112 and HST GO-15889, and STFC grants ST/T000198/1 and ST/S006109/1. The ATLAS science products have been made possible through the contributions of the University of Hawaii Institute for Astronomy, the Queen’s University Belfast, the Space Telescope Science Institute, the South African Astronomical Observatory, and The Millennium Institute of Astrophysics (MAS), Chile. We acknowledge with thanks the variable star observations from the AAVSO International Database contributed by observers worldwide and used in this research. This research made use of Astropy², a community-developed core Python package for Astronomy (Astropy Collaboration et al. 2013, 2018).

References

- Abdurro’uf, Accetta, K., Aerts, C., et al. 2022, *ApJS*, 259, 35
- Adams, S. M., Kochanek, C. S., Gerke, J. R., Stanek, K. Z., & Dai, X. 2017, *MNRAS*, 468, 4968
- Alcock, C., Allsman, R. A., Alves, D., et al. 1997, *ApJ*, 486, 697
- Alcock, C., Allsman, R. A., Alves, D. R., et al. 1999, *PASP*, 111, 1539
- Antoniadis, K., Bonanos, A. Z., de Wit, S., et al. 2024, *A&A*, 686, A88
- Anugu, N., Baron, F., Gies, D. R., et al. 2023, *AJ*, 166, 78
- Aret, A., Kraus, M., Kolka, I., & Maravelias, G. 2017, in *Astronomical Society of the Pacific Conference Series*, Vol. 510, *Stars: From Collapse to Collapse*, ed. Y. Y. Balega, D. O. Kudryavtsev, I. I. Romanyuk, & I. A. Yakunin, 162
- Aret, A., Kraus, M., & Šlechta, M. 2016, *MNRAS*, 456, 1424
- Astropy Collaboration, Price-Whelan, A. M., Sipőcz, B. M., et al. 2018, *AJ*, 156, 123
- Astropy Collaboration, Robitaille, T. P., Tollerud, E. J., et al. 2013, *A&A*, 558, A33
- Ballester, P., Modigliani, A., Boitquin, O., et al. 2000, *The Messenger*, 101, 31
- Beasor, E. R., Davies, B., Smith, N., et al. 2020, *MNRAS*, 492, 5994
- Beasor, E. R. & Smith, N. 2022, *ApJ*, 933, 41
- Beasor, E. R., Smith, N., & Jencson, J. E. 2024, *ApJ*, in press, (arXiv:2410.14027)
- Bergemann, M., Kudritzki, R.-P., Gazak, Z., Davies, B., & Plez, B. 2015, *ApJ*, 804, 113
- Bond, H. E., Henden, A., Levay, Z. G., et al. 2003, *Nature*, 422, 405
- Bonnell, I. A. & Bate, M. R. 2005, *MNRAS*, 362, 915
- Bordier, E., Frost, A. J., Sana, H., et al. 2022, *A&A*, 663, A26
- Calzoletti, L., Melandri, A., Testa, V., et al. 2005, *Nuovo Cimento C Geophysics Space Physics C*, 28, 759
- Chatys, F. W., Bedding, T. R., Murphy, S. J., et al. 2019, *MNRAS*, 487, 4832
- Chen, P., Gal-Yam, A., Sollerman, J., et al. 2024, *Nature*, 625, 253
- Cheng, S. J., Goldberg, J. A., Cantiello, M., et al. 2024, *ApJ*, 974, 270
- Chesneau, O., Meilland, A., Chapellier, E., et al. 2014, *A&A*, 563, A71
- Choi, J., Dotter, A., Conroy, C., et al. 2016, *ApJ*, 823, 102
- Cutri, R. M., Wright, E. L., Conrow, T., et al. 2021, *VizieR Online Data Catalog*, II/328
- Davies, B. & Beasor, E. R. 2020, *MNRAS*, 493, 468
- Davies, B., Plez, B., & Petrucci, M. 2022, *MNRAS*, 517, 1483
- De, K., MacLeod, M., Jencson, J. E., et al. 2024, arXiv e-prints, arXiv:2410.14778
- de Jager, C. 1998, *A&A Rev.*, 8, 145
- de Jager, C., Nieuwenhuijzen, H., & van der Hucht, K. A. 1988, *A&AS*, 72, 259
- de Wit, S., Bonanos, A. Z., Antoniadis, K., et al. 2024, *A&A*, 689, A46
- de Wit, S., Bonanos, A. Z., Trammer, F., et al. 2023, *A&A*, 669, A86
- Decin, L., Hony, S., de Koter, A., et al. 2006, *A&A*, 456, 549
- Decin, L., Richards, A. M. S., Marchant, P., & Sana, H. 2024, *A&A*, 681, A17
- Dekker, H., D’Odorico, S., Kaufer, A., Delabre, B., & Kotzłowski, H. 2000, in *Society of Photo-Optical Instrumentation Engineers (SPIE) Conference Series*, Vol. 4008, *Optical and IR Telescope Instrumentation and Detectors*, ed. M. Iye & A. F. Moorwood, 534–545
- Dotter, A. 2016, *ApJS*, 222, 8
- Dupree, A. K., Strassmeier, K. G., Calderwood, T., et al. 2022, *ApJ*, 936, 18
- Ekström, S., Georgy, C., Eggenberger, P., et al. 2012, *A&A*, 537, A146
- Elias, J. H., Frogel, J. A., & Schwing, P. B. W. 1986, *ApJ*, 302, 675
- Ercolino, A., Jin, H., Langer, N., & Dessart, L. 2024, *A&A*, 685, A58
- Evans, A., Geballe, T. R., Rushton, M. T., et al. 2003, *MNRAS*, 343, 1054
- Exter, K. M., Cox, N. L. J., Swinyard, B. M., et al. 2016, *A&A*, 596, A96

² <https://www.astropy.org>

- Folatelli, G., Bersten, M. C., Kuncarayakti, H., et al. 2015, *ApJ*, 811, 147
- Gaia Collaboration, Prusti, T., de Bruijne, J. H. J., et al. 2016, *A&A*, 595, A1
- Gaia Collaboration, Vallenari, A., Brown, A. G. A., et al. 2023, *A&A*, 674, A1
- Georgy, C. 2012, *A&A*, 538, L8
- Glatzel, W. & Kiriakidis, M. 1993, *MNRAS*, 263, 375
- Gordon, M. S. & Humphreys, R. M. 2019, *Galaxies*, 7, 92
- Grindlay, J., Tang, S., Smeice, R., et al. 2009, in *Astronomical Society of the Pacific Conference Series*, Vol. 410, *Preserving Astronomy's Photographic Legacy: Current State and the Future of North American Astronomical Plates*, ed. W. Osborn & L. Robbins, 101
- Groenewegen, M. A. T., Nanni, A., Cioni, M. R. L., et al. 2020, *A&A*, 636, A48
- Groenewegen, M. A. T., Sloan, G. C., Soszyński, I., & Petersen, E. A. 2009, *A&A*, 506, 1277
- Guinan, E. F., Wasatonic, R. J., & Calderwood, T. J. 2019, *The Astronomer's Telegram*, 13341, 1
- Heger, A., Fryer, C. L., Woosley, S. E., Langer, N., & Hartmann, D. H. 2003, *ApJ*, 591, 288
- Heger, A., Jeannin, L., Langer, N., & Baraffe, I. 1997, *A&A*, 327, 224
- Heinze, A. N., Tonry, J. L., Denneau, L., et al. 2018, *AJ*, 156, 241
- Houck, J. R., Roellig, T. L., Van Cleve, J., et al. 2004, in *Society of Photo-Optical Instrumentation Engineers (SPIE) Conference Series*, Vol. 5487, *Optical, Infrared, and Millimeter Space Telescopes*, ed. J. C. Mather, 62–76
- Hubble, E. & Sandage, A. 1953, *ApJ*, 118, 353
- Humphreys, R. M. & Davidson, K. 1979, *ApJ*, 232, 409
- Humphreys, R. M., Gordon, M. S., Martin, J. C., Weis, K., & Hahn, D. 2017, *ApJ*, 836, 64
- Humphreys, R. M., Helton, L. A., & Jones, T. J. 2007, *AJ*, 133, 2716
- Humphreys, R. M. & Jones, T. J. 2022, *AJ*, 163, 103
- Humphreys, R. M., Jones, T. J., & Gehrz, R. D. 1987, *AJ*, 94, 315
- Humphreys, R. M., Jones, T. J., & Martin, J. C. 2023, *AJ*, 166, 50
- Humphreys, R. M., Jones, T. J., Polomski, E., et al. 2006, *AJ*, 131, 2105
- Humphreys, R. M., Weis, K., Davidson, K., Bomans, D. J., & Burggraf, B. 2014, *ApJ*, 790, 48
- Ivanova, N., Justham, S., Chen, X., et al. 2013, *A&A Rev.*, 21, 59
- Jian, M., Matsunaga, N., Jiang, B., Yuan, H., & Zhang, R. 2024, *A&A*, 682, A59
- Kamiński, T., Tyłenda, R., Kiljan, A., et al. 2021, *A&A*, 655, A32
- Kelson, D. D. 2003, *PASP*, 115, 688
- Kelson, D. D., Illingworth, G. D., van Dokkum, P. G., & Franx, M. 2000, *ApJ*, 531, 159
- Khan, R., Stanek, K. Z., Kochanek, C. S., & Bonanos, A. Z. 2011, *ApJ*, 732, 43
- Klochova, V. G. 2019, *Astrophysical Bulletin*, 74, 475
- Koumpia, E., Oudmaijer, R. D., Graham, V., et al. 2020, *A&A*, 635, A183
- Kourmiotis, M., Bonanos, A. Z., Soszyński, I., et al. 2014, *A&A*, 562, A125
- Kourmiotis, M., Bonanos, A. Z., Yuan, W., et al. 2017, *A&A*, 601, A76
- Kourmiotis, M., Kraus, M., Maryeva, O., Borges Fernandes, M., & Maravelias, G. 2022, *MNRAS*, 511, 4360
- Kraus, M. 2019, *Galaxies*, 7, 83
- Kravchenko, K., Chiavassa, A., Van Eck, S., et al. 2019, *A&A*, 632, A28
- Kravchenko, K., Jorissen, A., Van Eck, S., et al. 2021, *A&A*, 650, L17
- Lamers, H. J. G. L. M., Zickgraf, F.-J., de Winter, D., Houziaux, L., & Zorec, J. 1998, *A&A*, 340, 117
- Landri, C. & Pejcha, O. 2024, *MNRAS*, 531, 3391
- Langer, N. 2012, *ARA&A*, 50, 107
- Levesque, E. M. 2017, *Astrophysics of Red Supergiants*
- Levesque, E. M., Massey, P., Olsen, K. A. G., & Plez, B. 2007, *ApJ*, 667, 202
- Levesque, E. M., Massey, P., Plez, B., & Olsen, K. A. G. 2009, *AJ*, 137, 4744
- Liimets, T., Kolka, I., Kraus, M., et al. 2023, *A&A*, 670, A13
- Lobel, A., Dupree, A. K., Stefanik, R. P., et al. 2003, *ApJ*, 583, 923
- MacLeod, M., Blunt, S., De Rosa, R. J., et al. 2024, *arXiv e-prints*, arXiv:2409.11332
- Mainzer, A., Bauer, J., Cutri, R. M., et al. 2014, *ApJ*, 792, 30
- Mainzer, A., Bauer, J., Grav, T., et al. 2011, *ApJ*, 731, 53
- Maravelias, G., de Wit, S., Bonanos, A. Z., et al. 2023, *Galaxies*, 11, 79
- Marshall, J. L., Bures, S., Thompson, I. B., et al. 2008, in *Ground-based and Airborne Instrumentation for Astronomy II*, ed. I. S. McLean & M. M. Casali, Vol. 7014, *International Society for Optics and Photonics (SPIE)*, 701454
- Marshall, J. R., van Loon, J. T., Matsuura, M., et al. 2004, *MNRAS*, 355, 1348
- Massey, P., Levesque, E. M., Olsen, K. A. G., Plez, B., & Skiff, B. A. 2007, *ApJ*, 660, 301
- McDonald, S. L. E., Davies, B., & Beasar, E. R. 2022, *MNRAS*, 510, 3132
- Meynet, G., Chomiene, V., Ekström, S., et al. 2015, *A&A*, 575, A60
- Meynet, G. & Maeder, A. 2003, *A&A*, 404, 975
- Mikołajewska, J. 2003, in *Astronomical Society of the Pacific Conference Series*, Vol. 303, *Symbiotic Stars Probing Stellar Evolution*, ed. R. L. M. Corradi, J. Mikołajewska, & T. J. Mahoney, 9
- Mikołajewska, J., Caldwell, N., Shara, M. M., & Iłkiewicz, K. 2015, *ApJ*, 799, L16
- Modigliani, A., Goldoni, P., Royer, F., et al. 2010, in *Society of Photo-Optical Instrumentation Engineers (SPIE) Conference Series*, Vol. 7737, *Observatory Operations: Strategies, Processes, and Systems III*, ed. D. R. Silva, A. B. Peck, & B. T. Soifer, 773728
- Montargès, M., Cannon, E., Lagadec, E., et al. 2021, *Nature*, 594, 365
- Moore, T., Smartt, S. J., Nicholl, M., et al. 2023, *ApJ*, 956, L31
- Munoz-Sanchez, G., de Wit, S., Bonanos, A. Z., et al. 2024, *A&A*, 690, A99
- Neugent, K. F., Levesque, E. M., Massey, P., & Morrell, N. I. 2019, *ApJ*, 875, 124
- Neugent, K. F., Levesque, E. M., Massey, P., Morrell, N. I., & Drout, M. R. 2020, *ApJ*, 900, 118
- Neugent, K. F., Massey, P., Skiff, B., & Meynet, G. 2012, *ApJ*, 749, 177
- Nieuwenhuijzen, H. & de Jager, C. 2000, *A&A*, 353, 163
- Nieuwenhuijzen, H., De Jager, C., Kolka, I., et al. 2012, *A&A*, 546, A105
- O'Connor, E. & Ott, C. D. 2011, *ApJ*, 730, 70
- Ohnaka, K., Driebe, T., Hofmann, K. H., Weigelt, G., & Wittkowski, M. 2008, *A&A*, 484, 371
- Ohnaka, K., Hofmann, K. H., Weigelt, G., et al. 2024, *A&A*, 691, L15
- Oudmaijer, R. D., Groenewegen, M. A. T., Matthews, H. E., Blommaert, J. A. D. L., & Sahu, K. C. 1996, *MNRAS*, 280, 1062
- Patrick, L. R., Thilker, D., Lennon, D. J., et al. 2022, *MNRAS*, 513, 5847
- Pietrzyński, G., Graczyk, D., Gállenne, A., et al. 2019, *Nature*, 567, 200
- Rayner, J. T., Cushing, M. C., & Vacca, W. D. 2009, *ApJS*, 185, 289
- Richards, A. M. S., Yates, J. A., & Cohen, R. J. 1996, *MNRAS*, 282, 665
- Sana, H., de Mink, S. E., de Koter, A., et al. 2012, *Science*, 337, 444
- Sana, H., Le Bouquin, J. B., Lacour, S., et al. 2014, *ApJS*, 215, 15
- Shingles, L., Smith, K. W., Young, D. R., et al. 2021, *Transient Name Server AstroNote*, 7, 1
- Smartt, S. J. 2009, *ARA&A*, 47, 63
- Smartt, S. J. 2015, *PASA*, 32, e016
- Smette, A., Sana, H., Noll, S., et al. 2015, *A&A*, 576, A77
- Soker, N. 2015, *ApJ*, 800, 114
- Sokolovsky, K. V., Gavras, P., Karpelas, A., et al. 2017, *MNRAS*, 464, 274
- Solf, J. 1978, *A&AS*, 34, 409
- Soszyński, I., Udalski, A., Szymanski, M. K., others, K., & Poleski, R. 2009, *Acta Astron.*, 59, 239
- Sukhbold, T., Ertl, T., Woosley, S. E., Brown, J. M., & Janka, H. T. 2016, *ApJ*, 821, 38
- Tabernero, H. M., Dorda, R., Negueruela, I., & González-Fernández, C. 2018, *MNRAS*, 476, 3106
- Tonry, J. L., Denneau, L., Heinze, A. N., et al. 2018, *PASP*, 130, 064505
- Udalski, A., Kubiak, M., & Szymanski, M. 1997, *Acta Astron.*, 47, 319
- Udalski, A., Soszyński, I., Szymanski, M. K., et al. 2008, *Acta Astron.*, 58, 89
- Udalski, A., Szymański, M. K., & Szymański, G. 2015, *Acta Astron.*, 65, 1
- Van Dyk, S. D., Garnavich, P. M., Filippenko, A. V., et al. 2002, *PASP*, 114, 1322
- van Genderen, A. M., Lobel, A., Nieuwenhuijzen, H., et al. 2019, *A&A*, 631, A48
- van Genderen, A. M., Nieuwenhuijzen, H., & Lobel, A. 2015, *A&A*, 583, A98
- van Loon, J. T., Cioni, M. R. L., Zijlstra, A. A., & Loup, C. 2005, *A&A*, 438, 273
- van Loon, J. T., Hekkert, P. T. L., Bujarrabal, V., Zijlstra, A. A., & Nyman, L.-A. 1998, *A&A*, 337, 141
- van Loon, J. T., Zijlstra, A. A., Bujarrabal, V., & Nyman, L. Å. 2001, *A&A*, 368, 950
- Vernet, J., Dekker, H., D'Odorico, S., et al. 2011, *A&A*, 536, A105
- Westerlund, B. E., Olander, N., & Hedin, B. 1981, *A&AS*, 43, 267
- Wood, P. R., Whiteoak, J. B., Hughes, S. M. G., et al. 1992, *ApJ*, 397, 552
- Wright, E. L., Eisenhardt, P. R. M., Mainzer, A. K., et al. 2010, *AJ*, 140, 1868
- Yang, M., Bonanos, A. Z., Jiang, B., et al. 2023, *A&A*, 676, A84
- Zacharias, N., Monet, D. G., Levine, S. E., et al. 2004, in *American Astronomical Society Meeting Abstracts*, Vol. 205, *American Astronomical Society Meeting Abstracts*, 48.15
- Zapartas, E., de Wit, S., Antoniadis, K., et al. 2024, *A&A*, *subm.*, (arXiv:2410.07335)

Appendix A: Nebular emission

Forbidden nebular emission in WOH G64 has been detected since its first optical spectrum in the 1980s (Elias et al. 1986). We do not see any extended emission in the 2D spectrum image of MagE, hence it originates in the circumstellar environment of WOH G64. We measured the radial heliocentric velocity of the lines and separated the blue and red components of the double-peaked lines in Table A.1. We find an outstanding separation of $\sim 210 \text{ km s}^{-1}$ in [N II] and $\sim 100 \text{ km s}^{-1}$ in [S II] even when WOH G64 was a RSG. The enhanced ratios [N II]/H α and [S II]/H α in the UVES spectrum suggest N-rich material due to its stellar evolution and shocks as the emission mechanism. We discarded the Keplerian disk origin because a rotation of $\sim 100 \text{ km s}^{-1}$ at the edge of a RSG atmosphere of $1500 R_{\odot}$ would imply a mass of $\sim 90 M_{\odot}$, which is far from the $25 M_{\odot}$ initial mass estimated for WOH G64 (Ohnaka et al. 2008). Bipolar outflows creating shocks with the material around WOH G64 might explain the origin of the double-peaked emission. However, Levesque et al. (2009) obtained a spectrum only one year after our UVES spectrum (see Table 2), they found single-peaked [N II] $\lambda 6584$ and [S II] $\lambda 6731$ with a RV in agreement with our red peak. Although the low spectral resolution ($\sim 150 \text{ km s}^{-1}$) prevented them from separating the double peak in [S II], we do not find an explanation for their apparent [N II] single peak.

The [Fe II] and the [Ca II] only appear after the transition of WOH G64 and the disappearance of the TiO band features, leading to the B[e]-star classification. The [O I] $\lambda 6300$ is the only forbidden line changing shape after the transition among the detected lines when WOH G64 was a RSG. The change from double to single-peak might indicate a different production mechanism of the line similar to the mechanism producing the single-peaked [Ca II] lines. We note that [O I] $\lambda\lambda 6300, 6364$ and [Ca II] $\lambda\lambda 7291, 7324$ typically arise in high-density environments, such as the inner-disc regions around B[e] supergiants (Aret et al. 2016).

Table A.1: Radial velocities of the forbidden lines and H β

Element	Wavelength (\AA)	UVES (km s^{-1})	X-Shooter (km s^{-1})	MagE (km s^{-1})	Element	Wavelength (\AA)	UVES (km s^{-1})	X-Shooter (km s^{-1})	MagE (km s^{-1})
H β_{blue}	4861.32	—	163 ± 1	146 ± 3	[S II] $_{\text{blue}}$	6716.44	—	207 ± 1	212 ± 5
H β_{red}	4861.32	—	375 ± 1	359 ± 3	[S II] $_{\text{red}}$	6716.44	—	309 ± 1	325 ± 3
[O III]	5006.84	—	—	294 ± 3	[S II] $_{\text{blue}}$	6730.81	216 ± 1	214 ± 1	231 ± 3
[N I] $_{\text{blue}}$	5197.90	—	263 ± 1	195 ± 1	[S II] $_{\text{red}}$	6730.81	321 ± 3	316 ± 1	339 ± 3
[N I] $_{\text{red}}$	5197.90	—	337 ± 1	336 ± 3	[Ca II]	7291.47	—	272 ± 1	270 ± 3
[O I]	6300.30	280 ± 1^a	274 ± 1	298 ± 3	[Ca II]	7323.89	—	272 ± 1	274 ± 3
[O I]	6363.78	—	260 ± 1	blended	[Fe II]	7155.17, 8616.95	—	268 ± 8	278 ± 5
[N II] $_{\text{blue}}$	6583.45	181 ± 1	183 ± 1	169 ± 3					
[N II] $_{\text{red}}$	6583.45	blended	391 ± 1	392 ± 3					

Notes. ^aThe center of the line is based on the broad component, ignoring the double-peaked shape.

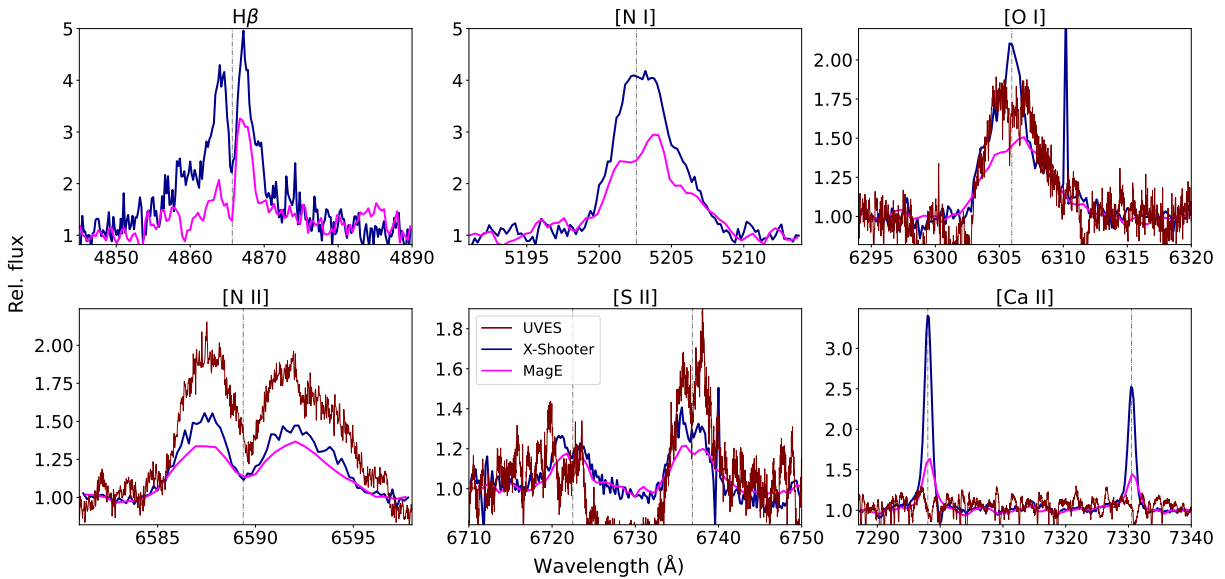


Fig. A.1: Comparison of the main forbidden lines between the UVES (brown), X-Shooter (blue), and MagE (magenta) spectra. The vertical grey dashed-dotted line indicates the center of the line assuming a RV of 270 km s^{-1} .

Appendix B: Spectral lines

Table B.1: Optical spectral lines of WOH G64 in the X-Shooter and MagE spectra

Wavelength (Å)	Ion	UVES	X-Shooter	MagE	Wavelength (Å)	Ion	UVES	X-Shooter	MagE
4068.60	[S II]	—	Em	Em	6141.73	Fe I	Abs	Em	Em
4340.46	H γ	—	Em	Em	6141.71	Ba II	x	x	Abs
4861.32	H β	—	double	double	6191.56	Fe I	x	Em	Em
4921.93	He I	—	Em	Em	6230.72	Fe I	x	Em	Em
5006.84	[O III]	—	x	Em	6247.56	Fe II	x	Em	Em
5018.44	Fe II	—	x	Abs	6252.56	Fe I	x	Em	Em
5019.73	Fe I	—	Em	x	6256.36	Ni I	x	Em	Em
5041.07	Fe I	—	Em	Em	6261.10	Ti I	Abs	x	x
5051.63	Fe I	—	Em	x	6280.62	Fe I	x	Em	Em
5079.90	?	—	x	Abs	6300.30	[O I]	Em	Em	Em
5079.74	Fe I	—	Em	x	6314.66	Ni I	x	Em	Em
5083.34	Fe I	—	Em	x	6318.02	Fe I	x	Em	x
5107.45	Fe I	—	Em	Em	6335.33	Fe I	x	Em	Em
5123.72	Fe I	—	Em	x	6347.11	Si II	x	x	Abs
5169.03	Fe II	—	x	Abs	6358.70	Fe I	x	Em	Em
5183.49	Fe I	—	Em	x	6363.78	[O I]	x	Em	Em
5183.81	Ti I	—	Em	x	6369.45	Fe II	x	Em	x
5185.90	Ti II	—	Em?	x	6371.37	Si II	x	x	Abs
5197.90	[N I]	—	Em	Em	6393.60	Fe I	x	Em	Em
5216.27	Fe I	—	Em	x	6400.32	Fe I	Abs	Em	Em
5227.15	Fe I	—	Em	x	6416.92	Fe II	x	Em	x
5234.62	Fe II	—	Em	x	6421.35	Fe I	Abs	x	Em
5066.78	?	—	Em	x	6432.67	Fe II	x	P-Cygni	Em
5269.54	Fe I	—	Em	x	6456.38	Fe II	x	Em	x
5270.36	Fe I	—	Em	x	6491.57	Ti II	x	Em	x
5273.37	Fe I	—	Em	x	6494.98	Fe I	x	Em	Em
5276.00	Fe II	—	Em	x	6496.90	Ba II	Abs	x	x
5283.62	Fe I	—	Em	x	6498.94	Fe I	x	Em	Em
5316.61	Fe II	—	Em	Abs?	6516.08	Fe II	x	Em	Em
5328.04	Fe I	—	Em	x	6548.05	[N II]	x	Em	Em
5341.02	Fe I	—	Em	x	6562.80	H α	double	double	P-Cygni
5367.65	?	—	Em	x	6572.78	Ca I	Abs	x	x
5371.49	Fe I	—	Em	x	6583.45	[N II]	double	double	double
5381.02	Ti II	—	Em?	Abs?	6592.91	Fe I	x	Em	Em
5366.69	?	—	Em	x	6649.80	?	Abs	Em	Em
5397.13	Fe I	—	Em	x	6663.44	Fe I	x	x	Em
5405.77	Fe I	—	Em	Em	6678.15	He I	x	Em	Em
5418.77	Ti II	—	Em	x	6716.44	[S II]	x	double	double
5429.70	Fe I	—	Em	x	6730.81	[S II]	double	double	double
5434.52	Fe I	—	Em	x	6743.12	Ti I	x	Em	Em
5446.92	Fe I	—	Em	x	6767.77	Ni I	x	Em	Em
5455.61	Fe I	—	Em	Em	6945.20	Fe I	x	x	Em
5526.78	Sc II	—	—	Abs	6999.88	Fe I	x	Em	Em
5577.37	?	—	Em	x	7091.50	?	x	Em	Em
5641.00	Sc II	—	—	Abs	7110.90	Ni I	x	Em	x
5641.01	Si II	—	—	Abs	7155.17	[Fe II]	x	Em	Em
5657.91	Sc II	—	—	Abs	7291.47	[Ca II]	x	Em	Em
5658.36	Sc II	—	—	Abs	7323.89	[Ca II]	x	Em	Em
5667.16	Sc II	—	—	Abs	7462.41	Fe II	x	Em	Em
5669.06	Sc II	—	—	Abs	7664.91	K I	—	Abs	Abs
5684.21	Sc II	—	—	Abs	7698.97	K I	Abs	Abs	Abs
5889.95	Na I	Abs	Abs	Abs	7711.72	Fe II	x	Em	Em
5895.92	Na I	Abs	Abs	Abs	7714.32	Ni I	x	Em	Em
5956.69	Fe I	x	Em	Em	7748.27	Fe I	x	x	Em
5991.37	Fe II	x	Em	Em	7774.17	O I	x	x	Abs
6065.48	Fe I	x	Em	Em	7788.94	Ni I	x	Em	Em
6084.10	Fe II	x	Em	Em	7912.87	Fe I	x	Em	Em
6108.12	Ni I	x	Em	Em	7978.82	Ti I	x	Em	Em
6128.94	?	x	x	Abs	8047.62	Fe I	Abs	Em	Em
6126.22	Ti I	x	x	Em	8068.24	Ti I	x	Em	Em
6137.69	Fe I	x	Em	Em	8075.15	Fe I	Abs	Em	Em

8183.26	Na I	Abs	x	x	8598.39	Pa11	x	Em	Abs
8194.82	Na I	Abs	x	x	8611.80	Fe I	Abs	x	Em
8327.06	Fe I	Abs	Em	Em	8616.95	[Fe II]	x	Em	x
8345.55	Pa20	x	x	Abs	8662.14	Ca II	Abs	double	P-Cygni
8359.00	Pa19	x	x	Abs	8665.02	Pa10	x	blended	blended
8387.77	Fe I	Abs	Em	Em	8674.75	Fe I	Abs	Em	Em
8374.48	Pa18	x	x	Abs	8675.37	Ti I	Abs	Em	Em
8392.40	Pa17	x	x	Abs	8688.50	Fe I	Abs	Em	Em
8413.32	Pa16	x	x	Abs	8692.33	Ti I	Abs	Em	Em
8434.95	Ti I	x	Em	Em	8735.04	?	x	Em	x
8437.96	Pa15	x	x	blended	8734.71	Ti I	Abs	Em	x
8446.36	O I	x	Em	Abs	8750.47	Pa9	x	Em	Abs
8467.25	Pa14	x	x	blended	8757.19	Fe I	Abs	x	Em
8498.02	Ca II	Abs	double	P-Cygni	8764.27	Fe II	x	Abs	x
8502.48	Pa13	x	blended	blended	8766.68	Ti I	Abs	Em	x
8514.07	Fe I	Abs	Em	Em	8806.76	Mg I	Abs	Em?	Em
8518.19	Ti I	Abs	Em	Em	8824.22	Fe I	Abs	Em	Em
8542.09	Ca II	Abs	double	P-Cygni	8862.78	Pa8	x	Em	Abs
8545.38	Pa12	x	blended	blended	8921.76	?	x	x	Abs
8582.91	Cr I	x	Abs	Em	9014.91	Pa7	x	Em	Abs
8582.91	Fe II	x	Em	x	9229.01	Pa6	x	Em	Abs

Notes. Emission lines are indicated with "Em", absorption lines with "Abs", P Cygni profiles with "P-Cygni", and double-peaked with "double". When the profile was irregular due to blending with other lines, we used the label "blended". The "x" indicates the absence of emission or absorption, while "—" means that the spectrum did not cover the line. We also report the observed wavelength of unidentified lines ("?").

Table B.2: Near-IR spectral lines of WOH G64 in the X-Shooter spectrum

Wavelength (μm)	Ion	X-Shooter	Wavelength (μm)	Ion	X-Shooter
0.95460	Pa ϵ	Em	1.26711	Ti I	Em
0.97182	[Fe II]	Em	1.27384	Ti I	Em
1.00494	Pa δ	Em	1.27450	Ti I	Em
1.03713	Si I	Abs	1.28037	Fe I	Em
1.03968	Ti I	Em	1.28181	Pa β	Em
1.03979	[N I]	Em	1.28314	Ti I	Em
1.04074	[N I]	Em	1.28470	Ti I	Em
1.04961	Ti I	Em	1.29200	Ti I	Em
1.05846	Ti I	Em	1.30119	Ti I	Em
1.06034	Si I	Abs	1.30773	Ti I	Em
1.06077	Ti I	Em	2.17829	Ti I	Em
1.06616	Ti I	Em	2.18974	Ti I	Em
1.06770	Ti I	Em	2.20045	Ti I	Em
1.07263	Ti I	Em	2.22328	Ti I	Em
1.07329	Ti I	Em	2.22740	Ti I	Em
1.07747	Ti I	Em	2.23106	Ti I	Em
1.08303	He I	Em	2.24439	Ti I	Em
1.09381	Pa γ	Em	2.08396	?	Em
1.16076	Fe I	Em	2.10527	?	Em
1.16383	Fe I	Em	2.11290	?	Em
1.16900	Fe I	Em	2.15031	?	Em
1.17833	Fe I	Em	2.15165	?	Em
1.18828	Fe I	Em	2.16040	?	Em
1.19495	Ti I	Em	2.18562	?	Em
1.19842	Si I	Abs	2.20690	?	Em
1.19916	Si I	Abs	2.20973	?	Em
1.21035	Si I	Abs	2.24386	?	Em
1.22707	Si I	Abs	2.25897	?	Em
1.25668	[Fe II]	Em	2.26462	?	Em
1.25668	Ti I	Em			

Notes. The notation is identical to that in Table B.1.

Appendix C: Optical spectral regions after the transition

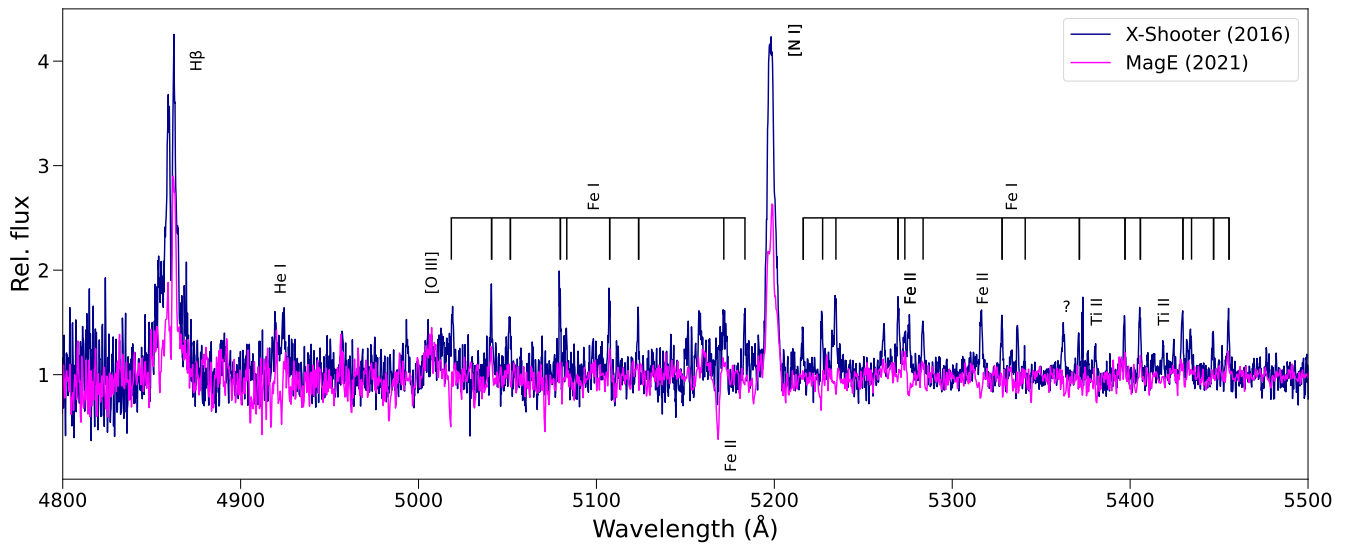


Fig. C.1: Comparison of the X-Shooter (dark blue) and MagE (magenta) spectra of WOH G64 between 4800-5500 Å with the main lines indicated.

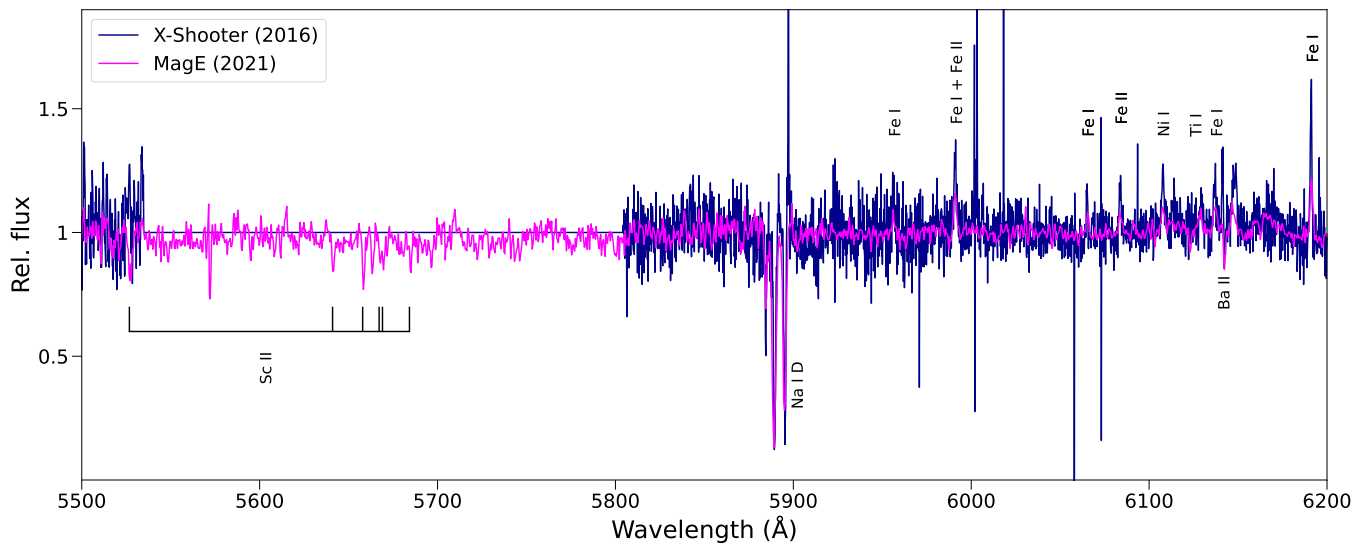


Fig. C.2: Same as Fig. C.1, but for 4800-5500 Å. The overlapping region between the UVB and Vis arms (5500-5810 Å) of the X-Shooter spectrum is not shown, due to its high noise.

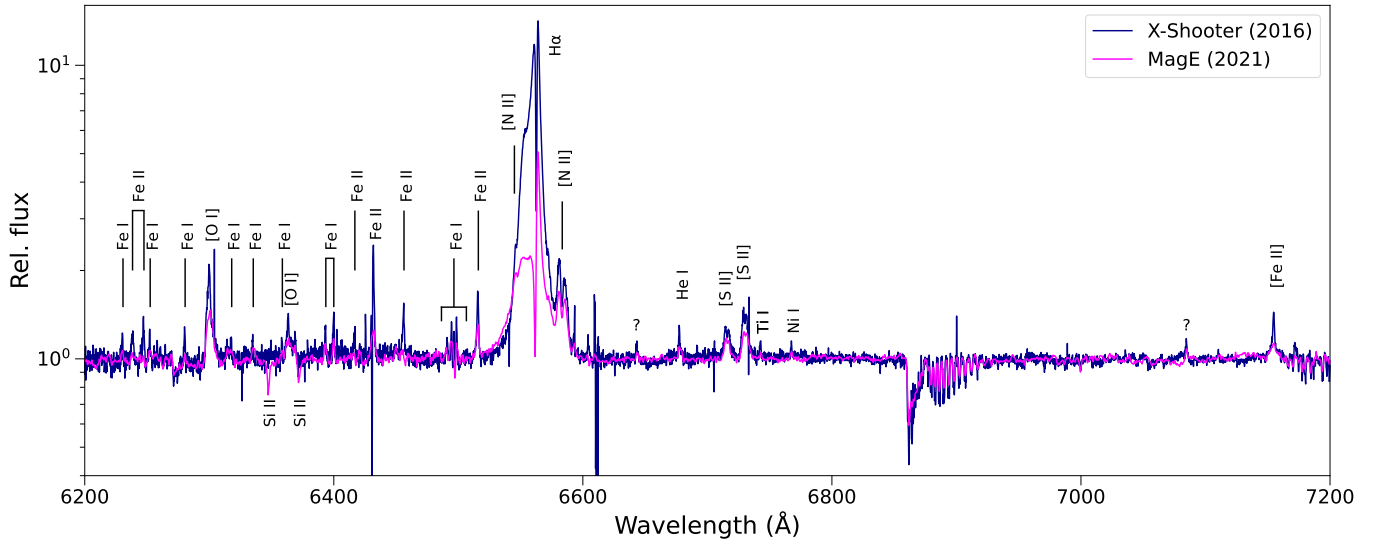


Fig. C.3: Same as Fig. C.1, but for 6200-7200 Å.

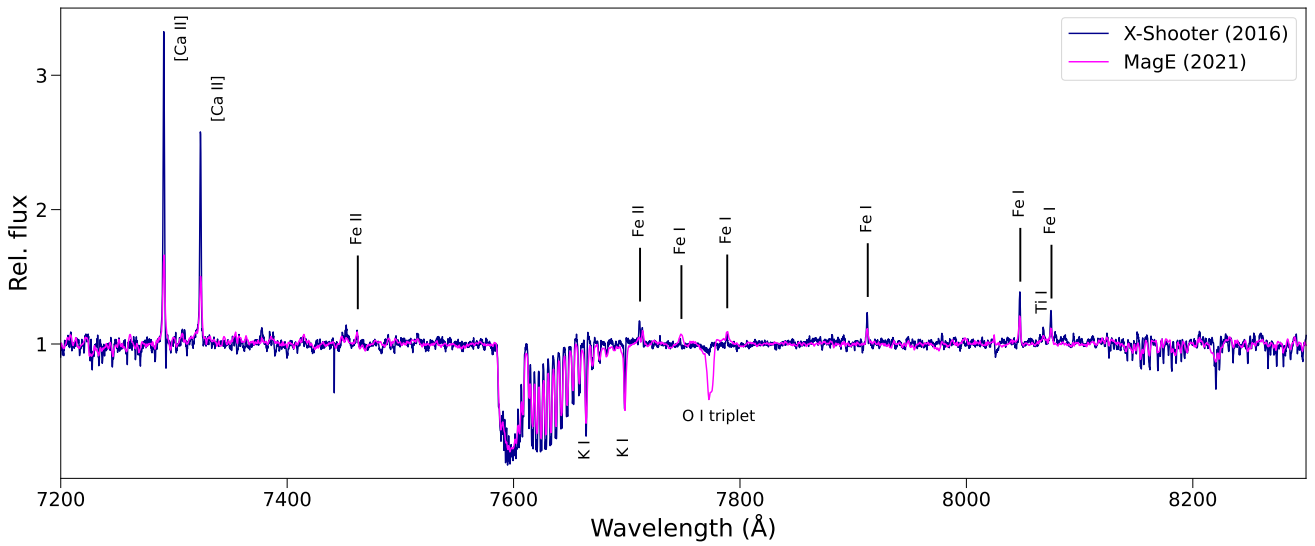


Fig. C.4: Same as Fig. C.1, but for 7200-8300 Å.

Appendix D: Near-IR spectrum from X-Shooter

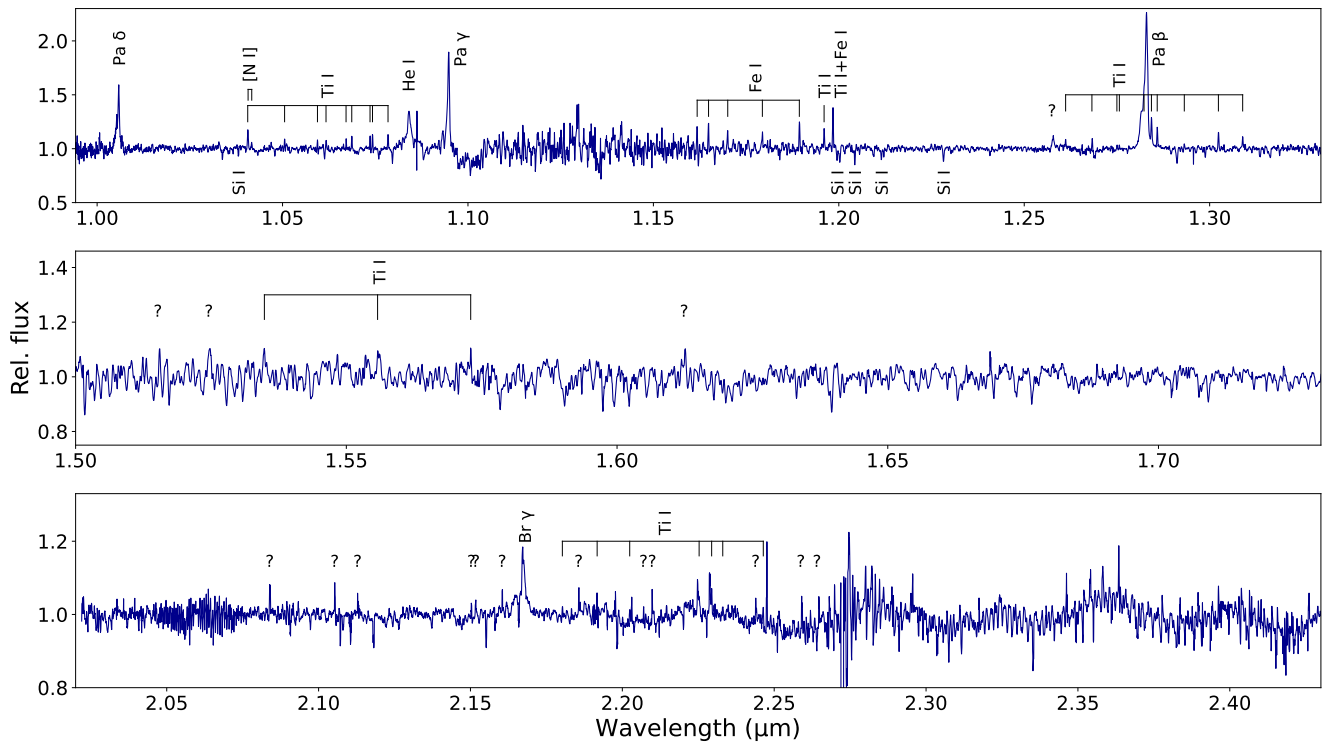


Fig. D.1: Normalized X-Shooter spectrum of WOH G64 in *YJ*-band (*top*), *H*-band (*middle*) and *K*-band (*bottom*), indicating identified lines. Unidentified lines are marked with a '?'.